Development and Validation of a Poroelastic Finite Element model of a human Lumbar Spine Segment

By

Nishant Bazzad

Thesis
Submitted to Flinders University
for the degree of

Bachelor of Engineering (Mechanical) (Honours) / Master of Engineering (Biomedical)

College of Science and Engineering
19/10/2023

TABLE OF CONTENTS

TABLE OF CONTENTS ..... **I**
EXECUTIVE SUMMARY ..... **III**
DECLARATION ..... **IV**
ACKNOWLEDGEMENTS ..... **V**
LIST OF FIGURES ..... **VI**
LIST OF TABLES ..... **VIII**
LIST OF SYMBOLS AND ABBREVIATIONS ..... **IX**
1. INTRODUCTION **1**
2. LITERATURE REVIEW **4**
2.1. Constitutive Equations 4
2.2. Material Properties 6
2.3. Calibration 6
2.4. Element Types 7
2.5. Boundary and Loading Conditions 9
2.6. Verification 10
2.7. Validation 11
3. METHODOLOGY **13**
3.1. Software 13
3.2. Original Model 13
3.3. Model Preparation 16
3.4. Poroelastic Behaviour Implementation 19
3.5. Boundary and Loading Conditions 21
3.6. Outputs 22
3.7. Post-Processing 23
4. VERIFICATION **24**
4.1. Study 1: Galbusera 24
4.1.1. Methodology 24
4.1.2. Results 24
4.1.3. Discussion 26
4.2. Study 2: Ferguson 28
4.2.1. Methodology 28
4.2.2. Results 29
4.2.3. Discussion 30
4.3. Study 3: Schmidt 31

4.3.1. Methodology 31
4.3.2. Results 32
4.3.3. Discussion 34
5. VALIDATION 36
5.1. Methodology 36
5.2. Results 36
5.3. Discussion 37
6. CONCLUSIONS 39
7. FUTURE WORK 40
8. BIBLIOGRAPHY 41
9. APPENDICES 45
Appendix A: Gantt chart 45
Appendix B: Literature Review 46
Appendix B1: Material properties 46
Appendix B2: Supplementary Section for Chapter 2.3. Calibration 48
Appendix C: MATLAB Script for creating Node and Element Sets 49
Appendix D: Python Scripts for Post Processing 56

EXECUTIVE SUMMARY

Low back pain is a significant problem that affects 580 million people around the world. Finite element (FE) models are used to analyse the biomechanics of the lumbar spine, which can be used to understand the injury mechanisms. An FE model of the L1-L2 functional spinal unit (FSU) was created in a previous study, with the geometry based on an experimental specimen that had undergone testing in 11 loading directions. This model neglected the time-dependent behaviour due to the fluid-dependent poroelasticity. Direct validation is where the FE model closely matches the experimental specimen, and the FE results are directly compared to the experimental results for the same specimen. No studies in the literature have directly validated a FE model of the lumbar FSU in 11 loading directions. The aim of this project was to implement poroelastic behaviour in the FE model of the L1-L2 FSU, verify the model against literature and directly validate the model in 11 loading directions. In the FE model of the L1-L2 FSU, the poroelastic behaviour was implemented on the intervertebral disc (IVD). To simulate the osmotic behaviour, a boundary pore pressure was prescribed on the boundary of the IVD which forced the flow of fluid to maintain this pressure. The FE model was verified against three studies that focused on different aspects of the model including the osmotic behaviour, loading behaviour and pore pressure distribution. Significant discrepancies were found between the FE model and literature, which were due to the various limitations of the FE model. The FE model was directly validated against the experimental results during the 12-hour axial compressive preload, where the axial displacement of the L1 vertebrae had a significantly different initial response, however the results were in reasonable agreement at the end of the preload. Due to the time constraints of the project and the steep learning curve for the author, the final model was not able to be directly validated in 11 loading directions. However, this project laid the foundations for directly validating the model in 11 loading directions, which has various future applications including the simulation of IVD degeneration.

DECLARATION

I certify that this thesis:

1. does not incorporate without acknowledgment any material previously submitted for a degree or diploma in any university
2. and the research within will not be submitted for any other future degree or diploma without the permission of Flinders University; and
3. to the best of my knowledge and belief, does not contain any material previously published or written by another person except where due reference is made in the text.

Signature of student: .....

Print name of student: Nishant Bazzad

Date: 19/10/2023

I certify that I have read this thesis. In my opinion it is/is not (please circle) fully adequate, in scope and in quality, as a thesis for the degree of **Bachelor of Engineering (Mechanical) (Honours) / Master of Engineering (Biomedical)**. Furthermore, I confirm that I have provided feedback on this thesis and the student has implemented it minimally/partially/fully (please circle).

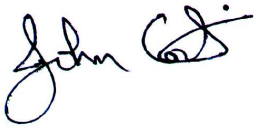

Signature of Principal Supervisor: .....

Print name of Principal Supervisor: John Costi

Date: 19/10/2023

ACKNOWLEDGEMENTS

I am extremely grateful to my academic supervisors including Associate Professor John Costi, Professor Mark Taylor and Associate Professor Paige Little (Queensland University of Technology) who have provided invaluable assistance during my project. I am especially grateful to Associate Professor John Costi who has provided the experimental data from the Flinders University Hexapod robot, has provided very detailed feedback for my drafts and has given unique biomechanical perspectives on Finite Element issues.

I am also deeply indebted to Professor Mark Taylor, who has provided critical support for my Finite Element issues and has allowed me to understand how to write about Finite Element in an academic manner. I am also extremely grateful to Associate Professor Paige Little who has provided the original Finite Element model, given invaluable assistance in understanding the model and has given vital support for my Finite Element issues. This has been a challenging project, but all of my academic supervisors have allowed me to do my best and I am deeply indebted to them.

I am thankful to Dr. Kieran Bennett who has provided assistance for problems encountered in the Finite Element model. I am also grateful to Aaron Baker who originally got me interested in Finite Element analysis many years ago. I would like to acknowledge both of my parents, who have always pushed me to do my best and have provided the emotional and financial support in order to make my studies possible. I would also like to thank my brother who has always been there to listen to my problems, and has pushed me through the toughest of times.

LIST OF FIGURES

Figure 1: Structure of the FSU in sagittal view. Note that ALL represents anterior longitudinal ligament and PLL represents posterior longitudinal ligament. The facet joint is enclosed by the capsular ligament. Adapted from Newell et al. (2017). Reused under a Creative Commons Attribution license. 1

Figure 2: Structure of the IVD, where CEP is cartilaginous endplates and BEP is bony endplates. Adapted from Newell et al. (2017). Reused under a Creative Commons Attribution license. 1

Figure 3: Original finite element model. Photo by the author based on the original model by Little and Adam (2012). 2

Figure 4: The 11 loading directions used for experimental testing. Adapted from Chang et al. (2011). Reused under a Creative Commons Attribution license. 2

Figure 5: Original FE model of the IVD, with the section A-A taken through the mid-sagittal plane. 14

Figure 6: The different types of constraints imposed on the FE model. 16

Figure 7: Original node set for the IVD, where nodes are defined within the annulus and nucleus cavity. 17

Figure 8: Node sets created for the nucleus and annulus. 17

Figure 9: Node set for the nucleus, which had 7 horizontal layers with each layer having the same layout of nodes. 18

Figure 10: (a) Cross-sectional view of the bottom layer. (b) Element shapes created manually, where elements with a poor shape are highlighted with a red circle. 18

Figure 11: Final FE model of the IVD, with the section B-B taken through the mid-sagittal plane. 19

Figure 12: Boundary and loading conditions of the (a) Experimental testing protocols and (b) FE model. The image in (a) was adapted from Asaad et al. (2020), reused under a Creative Commons Attribution license. 22

Figure 13: Location of the outputs used in this project. A: Centre of IVD superior surface. B: Centre of IVD inferior surface. C: Centre of nucleus. D: Inner anterior annulus. E: Outer anterior annulus. F: Lateral annulus. 22

Figure 14: Flow chart for the scripting used to post-process the Abaqus results. 23

Figure 15: Pore pressure in the centre of the nucleus during the 8 hours of free swelling. Results approximated from Galbusera et al. (2011c). 25

Figure 16: Change in volume of the nucleus and annulus relative to the initial state, during the 8 hours of free swelling. Results approximated from Galbusera et al. (2011c). 25

Figure 17: Axial (z) displacement of the centre of the IVD superior surface during the 8 hours of free swelling. Note that positive displacement represents movement superiorly. Results approximated from Galbusera et al. (2011c). 25

Figure 18: Lateral (y) displacement of the lateral annulus during the 8 hours of free swelling. Note that negative displacement represents movement laterally. Results approximated from Galbusera et al. (2011c). 25

Figure 19: Load history of the axial compressive load applied to the superior surface of the L1 vertebrae, during the verification against Ferguson et al. (2004). 28

Figure 20: Change in IVD height over Day 2. Note that the change in IVD height has been normalised with respect to the end of the Day 2 Rest period (At 32 hours). Results approximated from Ferguson et al. (2004). 29

Figure 21: Load history for the axial compressive load applied to the superior surface of the L1 vertebrae, replicating the loading conditions of Schmidt et al. (2011). 31

Figure 22: Contour plots for the pore pressure distribution of the final model. The path of nodes used to obtain the outputs of pore pressure can be seen in the bottom right, with the results shown in Figure 23. 32

Figure 23: Pore pressure obtained along a path of nodes as shown in Figure 22, where the vertical height is from the centre of the IVD inferior surface. This is obtained at the start of the Day 2 Rest (Immediately after unloading) and start of Day 2 Loading (immediately after loading). 32

Figure 24: Pore pressure in the centre of the nucleus during Day 2. Results approximated from Schmidt et al. (2011). 32

Figure 25: Axial (z) displacement of the centre of the nucleus during the Day 2 Rest period. Note that the displacement has been zeroed at 24 hours, and positive displacement represents movement superiorly. Results approximated from Schmidt et al. (2011). 33

Figure 26: Axial (z) displacement of the centre of the nucleus during the Day 2 Loading period. Note that the displacement has been zeroed at 32 hours, and positive displacement represents movement superiorly. Results approximated from Schmidt et al. (2011). 33

Figure 27: Axial displacement of the L1 vertebrae during the 12-hour axial compressive preload. Note that negative axial displacement represents movement inferiorly. Experimental results provided by Amin (2019). 36

Figure 28: Timeline for the project. 45

LIST OF TABLES

Table 1: Loading directions used for validation by various FE models in the literature. The material behaviour that is used in each study is shown in the "Material Behaviour" column, where "P" represent poroelastic material behaviour and "PH" represents porohyperelastic material behaviour. For the types of validation, "I" represents indirect validation whereas "D" represents direct validation. 12

Table 2: Material properties and element types used to model all tissues in the original model. The material properties for the nucleus include the fluid density ($\boldsymbol{\rho}$), whereas for the annulus bulk include the coefficients of the strain energy potential equation $\boldsymbol{C10}$, $\boldsymbol{C01}$ and $\boldsymbol{D1}$ (Little and Adam, 2012). 14

Table 3: Material properties and element types, used to model all tissues in the final model. The absolute permeability for both the nucleus and annulus was specified as $\boldsymbol{k}$ = 7.5E-16 m^4/Ns and this was used to calculate the specific permeability as shown in the table. The elastic modulus, poisson's ratio, absolute permeability and initial voids ratio were derived from Ferguson et al. (2004), whereas the specific weight was derived from Silva et al. (2005). 20

Table 4: The material behaviour used in each study as well as for each individual tissue is shown, where "E" represents elastic material behaviour, "P" represent poroelastic material behaviour and "PH" represents porohyperelastic material behaviour. A dash ("-") indicates that the information is not available, since the information was not reported in the study. 46

LIST OF SYMBOLS AND ABBREVIATIONS

Pa	Pascal
E	Elastic modulus
v	Poisson's ratio
σ	Normal stress
σ_T	Total stress
σ_E	Effective solid stress
p	Pore fluid pressure
∇p	Spatial gradient of pore fluid pressure
I	Identity matrix
$\overline{v}$	Fluid velocity
k	Permeability
k_o	Initial permeability
M	Experimental matching factor
e	Voids ratio
e_o	Initial voids ratio
n	Porosity
n_i	Initial porosity
J	Volumetric strain
V	Volume
V_o	Initial volume

1. INTRODUCTION

Low back pain is a significant problem that affects approximately 580 million people around the world, that represents 7.5% of the global population (Williamson and Cameron, 2021). In Australia alone, approximately $4.8 billion (AUD) dollars is spent every year managing low back pain (Australian Commission on Safety and Quality in Healthcare, 2022). Degenerative disc disease and lumbar disc herniation are the most common causes of low back pain, with approximately 95% of all lumbar disc herniation occurring in the spine segments of L4-L5 and L5-S1 (Al Qaraghli and De Jesus, 2023). It is important to have a fundamental understanding of the lumbar spinal segments, since this can be used to analyse the load distribution and injury mechanisms (Adams and Dolan, 2005).

The L1-L2 functional spinal unit (FSU) consists of the intervertebral disc (IVD), inferior and superior vertebral bodies, posterior structures, facet joints and seven major ligaments (Figure 1). The seven ligaments include the anterior longitudinal ligament, posterior longitudinal ligament, interspinous ligament, supraspinous ligament, inter-transverse ligament, ligamentum flavum and capsular ligament (Newell et al., 2017). The facet joint is a synovial joint that allows posterolateral articulation between adjacent vertebral bodies and it is composed of a synovial membrane, hyaline cartilage and fibrous capsule (Cohen and Raja, 2007).

The IVD consists of three components including the nucleus pulposus (nucleus), annulus fibrosis (annulus) and cartilaginous endplates (CEP) which are bound to the bony endplates (BEP) on the adjacent vertebral bodies (Figure 2). The nucleus is a gelatinous structure, which is responsible for creating the hydrostatic pressure within the IVD. The annulus are concentric layers which surround the nucleus, enabling the IVD to bear tensile circumferential stresses. The CEP are thin layers of hyaline cartilage, which binds the IVD to the BEP which are thin layers of cortical bone on the vertebral bodies (Newell et al., 2017).

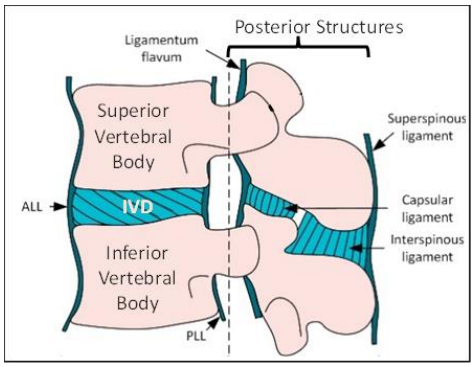

Figure 1: Structure of the FSU in sagittal view. Note that ALL represents anterior longitudinal ligament and PLL represents posterior longitudinal ligament. The facet joint is enclosed by the capsular ligament. Adapted from Newell et al. (2017). Reused under a Creative Commons Attribution license.

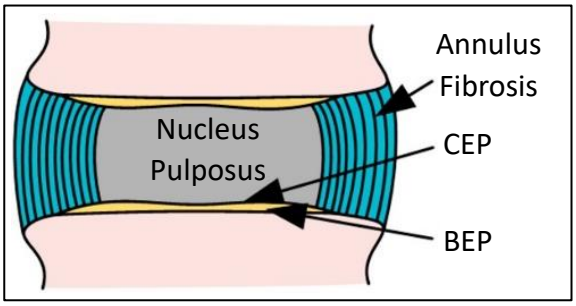

Figure 2: Structure of the IVD, where CEP is cartilaginous endplates and BEP is bony endplates. Adapted from Newell et al. (2017). Reused under a Creative Commons Attribution license.

Various techniques are used to analyse the biomechanics of the lumbar spine, including *in vitro* and *in vivo* experimental techniques as well as computational finite element (FE) models (Adams and Dolan, 2005). FE models offer several advantages over experimental techniques, including their ability to iteratively modify parameters while also reducing the need for experimental testing (Dreischarf et al., 2014).

A three-dimensional model of the L1-L2 functional spinal unit (FSU), was created on the commercial FE program Abaqus (2019, Dassault Systèmes, Waltham, MA, USA) by researchers at the Queensland University of Technology (Figure 3) (Little and Adam, 2012). This was a patient-specific model, with the geometry based on imaging data obtained from a cadaver L1-L2 FSU specimen at Flinders University (Amin, 2019). Computed tomography (CT) scans were used to construct the geometry (Little and Adam, 2012).

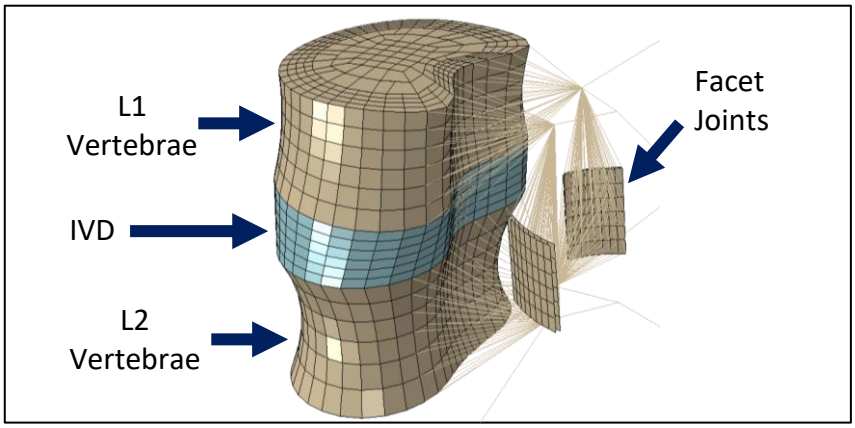

Figure 3: Original finite element model. Photo by the author based on the original model by Little and Adam (2012).

This same L1-L2 FSU specimen was then experimentally tested in each of the six degrees of freedom using the Hexapod robot at Flinders University. The experimental tests were conducted in 11 loading directions: anterior shear, posterior shear, left lateral shear, right lateral shear, left axial rotation, right axial rotation, left lateral bending, right lateral bending, flexion, extension and compression (Figure 4) (Amin, 2019).

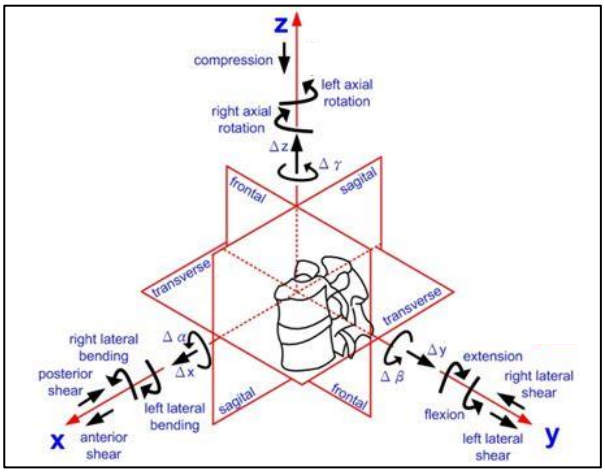

Figure 4: The 11 loading directions used for experimental testing. Adapted from Chang et al. (2011). Reused under a Creative Commons Attribution license.

The experimental testing sequence initially applied a 12-hour axial compressive preload equivalent to a nucleus pressure of 0.1MPa, which allowed the disc to achieve equilibrium hydration levels. For each of the 11 loading directions, the following dynamic loading and recovery sequence was repeated: haversine 1Hz (5 cycles), haversine 0.1Hz (5 cycles), haversine 0.01Hz (5 cycles), recovery (10 minutes), haversine 0.001Hz (2 cycles), recovery (10 minutes), stress relaxation (5 minutes), recovery (10 minutes) and creep (5 minutes). The 10 minutes recovery period was sufficient for returning the IVD to the equilibrium hydration levels. The results that were obtained from the experimental testing included force-displacement data for the entire FSU, as well as internal maximum shear strain at 173 nodes across the transverse cross-section of the IVD (Amin, 2019).

In the original FE model, various simplifying assumptions are made to model the IVD. The IVD is modelled using nonlinear hyperelastic behaviour. However, the original model neglects the time-dependent behaviour which is present in the IVD due to both intrinsic solid-phase viscoelasticity and fluid-dependent poroelasticity. The intrinsic viscoelasticity is due to the stretching and sliding of the collagen fibrils, whereas the poroelasticity is due to the flow of interstitial water through the porous tissue matrix (Bezci et al., 2020). The original FE model has undergone preliminary validation in limited loading directions.

The aims of this project are to implement poroelastic behaviour on the FE model of the L1-L2 FSU, verify the model with results from literature and directly validate the model against experimental results in 11 loading directions. The project proposes the hypothesis: The FE model with poroelastic properties will have close alignment with the results from the literature and the experimental results.

Initially, a literature review was conducted which explored the methodologies and techniques used to simulate poroelastic behaviour in FE models of the lumbar FSU. The findings from the literature review, were used to inform the methodology used in this project. In the FE model of the L1-L2 FSU, the poroelastic material properties were implemented on the IVD using Abaqus. The FE model was verified against three studies which focused on different aspects of the model including the swelling behaviour, loading behaviour and the pressure distribution throughout the IVD. The FE model was then validated against the experimental results, during the axial compressive preload for 12 hours. The timeline for the project can be seen in Appendix A: Gantt Chart, with the literature review lasting for 7 weeks, model development lasting for 10 weeks, post-processing lasting for 2 weeks, model verification lasting for 4 weeks and model validation lasting for another 2 weeks. The model development took significantly longer than expected, which pushed back the timeline significantly and limited the validation that could be performed.

2. LITERATURE REVIEW

FE models have been used extensively over the last two decades to model the lumbar spine, which includes full L1-L5 models (Dreischarf et al., 2014) and individual FSU models (Galbusera et al., 2011c). FE models of the lumbar spine use a range of theories to describe the mechanical behaviour of tissues which includes elastic, hyperelastic, viscoelastic, poroelastic, porohyperelastic and poroviscoelastic (Oftadeh et al., 2018). For the lumbar FSU, several FE models have been developed which include poroelastic behaviour (Natarajan et al., 2007).

The most commonly used FE solvers in modelling poroelastic behaviour for lumbar FSU are commercial based, with Abaqus (2023, Dassault Systèmes, Waltham, MA, USA), and open source software, FEBio (4.1, Musculoskeletal Research Laboratories, University of Utah, Salt Lake City, UT, USA) (Galbusera et al., 2014). When simulating poroelastic tissues, Abaqus uses the soil consolidation theory whereas FEBio uses the mixture theory of porous media (Meng et al., 2013). Although these programs use different approaches to model poroelastic material behaviour, the results from both for biomechanical applications are very similar (Galbusera et al., 2014).

By default, Abaqus and FEBio both allow modelling of frictionless contact between two saturated porous tissues. When the tissues remain in constant contact with each other, almost identical results are found between the default algorithms on Abaqus and FEBio. However, if the tissues undergo separation, then the default algorithm on Abaqus can lead to unrealistic simulations at the interface, compared to FEBio which performs relatively well. An iterative user-defined subroutine on Abaqus has been found to yield comparable results to FEBio, however this requires programming effort (Galbusera et al., 2014).

2.1. Constitutive Equations

The poroelastic formulation on Abaqus, assumes that the porous medium is composed of a solid matrix fully saturated by an interstitial fluid. This results in two unknown field variables including solid displacement and pore pressure, which is referred to as the $u - p$ (displacement-pressure) formulation (Argoubi and Shirazi-Adl, 1996). This uses the effective stress principle known as Biot's consolidation theory (Stokes et al., 2010). The effective stress principle states that the total stress on a poroelastic tissue, is composed of the stress in the solid matrix and the hydrostatic pressure of the pore fluid (Cheung et al., 2003). The effective stress of the solid matrix σ_E can be calculated using

equation (1), which is a function of the total stress σ_T, pore fluid pressure p and identity matrix I (Dassault Systèmes., 2022a).

$$\sigma_E = \sigma_T + pI \quad (1)$$

The effective solid matrix stress σ_E has a linear relationship with the relative nodal displacements, whereas the pore pressure p has a linear relationship with the fluid velocity (Stokes et al., 2010). The solid matrix can use any of the mechanical constitutive models available on Abaqus including elastic, hyperelastic and viscoelastic behaviour (Dassault Systèmes., 2022a). The constitutive behaviour of the fluid flow is governed using Darcy's law if the fluid has low flow velocity, or Forchheimer's law if the fluid has high flow velocity (Dassault Systèmes., 2022b). Poroelastic FE models of the lumbar FSU assume that the fluid has low flow velocity and therefore use Darcy's law. Darcy's law is shown in equation (2), which defines the fluid velocity $\overline{v}$ in terms of the tissue permeability k and spatial gradient of pore pressure ∇p (Ferguson et al., 2004).

$$\overline{v} = -k\nabla p \quad (2)$$

The tissue permeability k can either be assumed as a constant or be strain-dependent (Argoubi and Shirazi-Adl, 1996). The tissue permeability for hydrated soft tissues, has been shown to decrease exponentially with increasing strains (Schmidt et al., 2011). In Abaqus, the strain-dependent permeability is implemented using the formulation shown in equation (3), where k_o is the initial permeability, M is a factor used to match experimental results, e is the voids ratio and e_o is the initial voids ratio (Argoubi and Shirazi-Adl, 1996).

$$k = k_o \left[\frac{e(1+e_o)}{e_o(1+e)}\right]^2 \exp\left[M\left(\frac{1+e}{1+e_o} - 1\right)\right] \quad (3)$$

The voids ratio e is a function of the fluid fraction (porosity) n of the tissue as shown in equation (4) (Schmidt et al., 2011).

$$e = \frac{n}{1-n} \quad (4)$$

The porosity n depends on the deformation of the tissue as shown in equation (5), where J is the volumetric strain of the medium (dV/dV_o) and n_o is the initial porosity (Schmidt et al., 2011).

$$n = 1 - J^{-1}(1-n_o) \quad (5)$$

2.2. Material Properties

Assuming that the solid matrix has elastic behaviour, the material properties that need to be specified for poroelastic tissues include the elastic modulus (E), poisson's ratio (v), initial permeability (k_o), initial voids ratio (e_o), experimental matching factor (M) and initial porosity (n_o). The material properties for the nucleus, annulus bulk, annulus fibres, CEP, BEP, cortical bone and trabecular bone were obtained from seven studies as shown in Appendix B1. It should be noted that various material properties are not specified in different studies, due to the varying reporting standards used by each author. This includes the initial porosity n_o, which is only reported in a small number of studies including Malandrino et al. (2009).

The material properties used in the poroelastic formulation, varies considerably in the experimental literature due to the difficulties in soft tissue experimentation, specimen variability and inconsistent measurement techniques (Malandrino et al., 2009). This can be seen in Appendix B1, where individual material properties vary significantly between different studies. Depending on the assumptions used, studies also use different techniques to model the individual tissues of the lumbar FSU.

The tissues that are commonly modelled using poroelastic behaviour include the nucleus, annulus, CEP, BEP, cortical bone and trabecular bone. The solid phase of the nucleus and annulus is modelled using either elastic, hyperelastic or viscoelastic material behaviour. The annulus is modelled as a fibre-reinforced composite structure, where the orientation of the annulus fibres alternates either at a fixed $\pm 30^{o}$ from horizontal (Zheng et al., 2022), or changes depending on the location where the orientation is $\pm 24^{o}$ anteriorly and $\pm 46^{o}$ posteriorly (Schmidt et al., 2011). These annulus fibres can either be modelled as linear tension-only truss elements (Cheung et al., 2003), or have nonlinear behaviour using a Holzapfel-Gasser-Ogden material formulation (Zheng et al., 2022).

Some studies do not model the CEP (Ferguson et al., 2004), whereas other studies do not model the BEP (Argoubi and Shirazi-Adl, 1996; Cheung et al., 2003; Galbusera et al., 2011b). Although most studies assume that the cortical and trabecular bone has isotropic material properties, some studies including Malandrino et al. (2009) specify orthotropic material properties where the properties are specified in the three principal directions.

2.3. Calibration

Calibration is the process of adapting the FE model to match the experimental data (Schmidt et al., 2007). Various studies have performed calibration by varying the material properties. Malandrino et

al. (2009) performed calibration on the L3-L4 IVD, by parametrically varying individual material properties including the elastic modulus (nucleus and annulus) and initial permeability (nucleus, annulus, CEP and trabecular bone). The elastic modulus of the nucleus ranged from 1 MPa (healthy) to 1.66 MPa (highly degenerated), whereas the elastic modulus of the annulus ranged from 2.56 MPa (healthy) to 12.29 MPa (highly degenerated) (Malandrino et al., 2009).

The initial permeability for the nucleus, annulus, CEP and trabecular bone was selected from a range of values most commonly used in the literature for poroelastic FE models. An analysis of variance (ANOVA) was conducted to identify the effects of all 6 material properties on three loading directions including compression, flexion and axial rotation. The annulus elastic modulus was the most significant factor in all three loading directions, whereas the nucleus elastic modulus and CEP initial permeability played a critical role in compression (Malandrino et al., 2009). Algorithms used to optimise the poroelastic material properties, were compared between different studies in the literature. This can be found in Appendix B2: Supplementary Section for Chapter 2.3. Calibration.

A rating system was introduced by Schmidt et al. (2007) to quantify the accuracy of FE models in predicting experimental results. These ratings include insufficient agreement (FE results lie outside of minimum-maximum range of experimental results), sufficient agreement (results within minimum-maximum range), satisfactory agreement (results within one standard deviation), good agreement (result accuracy greater than 80%) and excellent agreement (result accuracy greater than 90%).

The accuracy of both the calibrated and non-calibrated models was compared in flexion (96.8% compared to 82.8%) and extension (93.8% compared to 77.1%), which showed that the calibrated model produced results with excellent agreement whereas the non-calibrated model had good agreement. Moreover, the accuracy of the calibrated and non-calibrated models was compared in simulating three different defect states, which showed that the calibrated model had excellent agreement for all defects, whereas the non-calibrated model had satisfactory or sufficient agreement. These results shows that although non-calibrated models produce results with good agreement for normal FSU, they are unable to accurately predict results for defect states which significantly limits the model's general applicability in simulating IVD degeneration (Schmidt et al., 2007).

2.4. Element Types

To model poroelastic tissues in Abaqus, FE models typically use pore pressure elements. The three-dimensional pore pressure elements include the 8-node hexahedral elements with trilinear

interpolation of displacement and pore pressure (C3D8P), as well as the 20-node hexahedral elements with triquadratic interpolation of displacement and trilinear interpolation of pore pressure (C3D20P) (Dassault Systèmes., 2022c). The C3D8P and C3D20P elements undergo full integration, where the number of Gauss integration points results in an exact solution of the element stiffness matrix. These elements can also be used with reduced integration (C3D8PR and C3D20PR), which feature one less Gauss integration point in each direction (Dassault Systèmes., 2022d).

For materials that are incompressible (poisson's ratio $= 0.5$) or close to incompressible (poisson's ratio > 0.475), the elements cannot undergo volume change which means that the pore pressure cannot be directly calculated from the nodal displacements. Hybrid elements have an extra degree of freedom at each node which directly calculates the pore pressure (Dassault Systèmes., 2022d), with hybrid formulations available for pore pressure elements with full integration (C3D8PH and C3D20PH) and reduced integration (C3D8RPH and C3D20RPH) (Dassault Systèmes., 2022c).

In a two-dimensional model of the S1-L1 lumbar spine, 8-node hybrid plane strain elements with reduced integration (CPE8RPH) were used. Testing the same model using non-hybrid plane strain elements (CPE8RP) had negligible effects on the results since the elastic properties for all tissues were far from incompressible, and it was concluded that hybrid elements were not required for this model (Zanjani-Pour et al., 2016).

In another study, a three-dimensional FE model of the IVD was created in a cylindrical shape, and 8-node and 20-node pore pressure elements with hybrid formulation and reduced integration (C3D8RPH and C3D20RPH) were analysed. The simulation time required to obtain solutions was significantly greater for the 20-node elements compared to the 8-node elements, being six times greater using an element size of 1mm and eleven times greater using an element size of 0.5mm. This was due to the significant increase in the total degrees of freedom, between the C3D8RPH and C3D20RPH elements (Stokes et al., 2010)

Various studies have used 20-node fully integrated C3D20P elements to mesh all tissues with poroelastic behaviour (Argoubi and Shirazi-Adl, 1996; Cheung et al., 2003; Schmidt et al., 2011), whereas other studies have used different element types depending on the tissue with C3D20P for the annulus, CEP, BEP and trabecular bone, whereas the hybrid C3D20PH is used for the nucleus (Hassan et al., 2021).

2.5. Boundary and Loading Conditions

Many experimental and FE investigations have assumed that the nucleus has a constant hydrostatic pressure, however studies have shown that the nucleus exhibits a substantial pressure gradient. These pressure gradients have been found to be larger in earlier cycles of dynamic loading, as well as at smaller applied preloads. Moreover, the fluid outflow from the nucleus is greater at the BEP compared to the annulus periphery (Schmidt and Shirazi-Adl, 2018).

For the lumbar FSU, multiple models have been used to simulate osmotic behaviour in the IVD including boundary pore pressure, fixed osmotic pressure (FOP), fixed osmotic pressure only in nucleus pulposus (FOP-N) and biphasic swelling (BS) models. The boundary pore pressure model simulates the osmotic behaviour by assigning a fixed pore pressure either to the boundary of the IVD (Galbusera et al., 2011c; Zanjani-Pour et al., 2016), or to all external surfaces of the IVD and vertebral bodies (Schmidt et al., 2011; Zheng et al., 2022). The fixed pore pressure ranges from 0.1-0.25MPa (Argoubi and Shirazi-Adl, 1996; Zanjani-Pour et al., 2016; Zheng et al., 2022), which can be implemented using the default definition fields available on Abaqus (Galbusera et al., 2011c).

The FOP and FOP-N models assign a fixed osmotic pressure gradient directly on the stress tensor. The BS model uses a simplified version of the Donnan effect, where the osmotic pressure gradient varies depending on the chemical potential and the volumetric deformation. For commercial FE programs including Abaqus, the FOP, FOP-N and BS models all require the use of user subroutines. The boundary pore pressure, FOP and FOP-N models were found to yield similar results and were acceptable approximations of the osmotic pressure behaviour. The BS model provided more accurate results, however this was significantly more difficult to implement (Galbusera et al., 2011c).

In compression loading after the load is removed (recovery phase), the poroelastic constitutive equations model a negative pressure within the IVD. This negative ‘suction-type’ pressure has not been reported *in vivo* during the recovery periods, and therefore this pressure is fictive in nature. This fictive pressure is caused by the large voids ratio of the nucleus and annulus, as well as the inherent constraints of having full saturation in the poroelastic constitutive equations. In order to minimise this negative suction-type pressure during the recovery phases, smaller voids ratio should be explored for the nucleus and annulus however this cannot be significantly different compared to the *in vivo* values. Moreover, sorption behaviour on Abaqus should be explored for the nucleus and annulus to allow for partial saturation (Schmidt et al., 2011).

A follower load is an axial compressive load that lies on the tangent of the curve of the lumbar spine, being used to replicate the loading conditions experienced *in vivo* (Patwardhan et al., 1999). This is simulated using thermo-isotropic truss elements, where the nodes are located on the bilateral cortical shell of the vertebral body and span across the IVD. These elements pass through the instantaneous centre of rotation for the FSU. By decreasing the temperature of the truss elements, the elements undergo contraction thereby creating a compressive load (Renner et al., 2007).

This magnitude of the compressive load can be found by fixing the inferior vertebrae, and calculating the reaction force on the truss elements. The follower preload created by the thermo-isotropic truss elements was then validated against *in vitro* experimental results, which showed good correlation with the experimental results. Compared to models without a follower pre-load, the follower preload was found to significantly decrease the range of motion in flexion-extension, lateral bending and torsion (Renner et al., 2007). An *in vitro* experimental study by Zirbel et al. (2013), also found that applying a follower preload increased the stiffness of the lumbar spine FSU in flexion-extension, lateral bending and torsion.

Poroelastic FE models loaded at rates of 1Hz, have been found to yield inaccurate results using a practical level of mesh refinement. This is due to the pressure fluctuations which can arise at free draining external boundaries and discontinuities between tissues. This can result in the minimum number of elements needed to obtain reliable results becoming prohibitively large, causing the model to exceed the computational random-access memory (RAM) available. Methods of preventing the pressure instabilities include using biased meshes, where the mesh is refined close to the external boundaries. Moreover, using 20 node pore pressure elements (C3D20RPH) compared to 8 node elements (C3D8RPH) has also been found to minimise the pressure fluctuations. However, these methods can be extremely computationally expensive and the results must be carefully checked in simulations involving rapid loading rates (Stokes et al., 2010).

2.6. Verification

The verification of the FE model is a crucial step in achieving reliable results (Xu et al., 2017). The verification of the FE model involves undertaking a mesh convergence study in order to optimise the mesh density. The parameters used for the mesh convergence should match the parameters of interest. Moreover, different parameters have been found to converge at different mesh densities, with gross results such as stiffness converging at smaller mesh densities compared to local results such as maximum strain (Jones and Wilcox, 2008). This was also found by Ayturk and Puttlitz (2011),

where the gross results (range of motion) converged at smaller mesh densities compared to the local results (strain energy density).

For gross results, the mesh density for a new model can be based on the mesh density for a previous model given that suitable evidence is present, however for local results a new convergence study must be undertaken. Mesh convergence has been achieved if increasing the mesh density, introduces less than a 5% difference in the parameters of interest (Jones and Wilcox, 2008). The convergence criterion varies between different studies, ranging from 2% (Schmidt et al., 2011) to 5% (Ayturk and Puttlitz, 2011; Campbell et al., 2016).

A mesh convergence analysis on the L1-L5 lumbar spine was conducted by Ayturk and Puttlitz (2011), where the sensitivity of each individual tissue to the changes in global mesh density was analysed. The mesh convergence was undertaken over various loading directions including flexion, extension, left/right lateral bending and left/right axial rotation. The convergence behaviour was found to be highly direction dependent, with lateral bending and axial rotation being the most sensitive to changes in mesh density (Ayturk and Puttlitz, 2011).

From the loading directions tested, axial rotation had the 'worst case' convergence behaviour and was recommended for use in mesh convergence studies to ensure conservative estimates. Moreover, minimal differences were found in the convergence behaviour of soft tissues (nucleus, annulus and CEP) compared to hard tissues (BEP, cortical bone and trabecular bone). For geometrically complex tissues including the posterior elements, it was recommended that the local results be analysed in addition to the global results to ensure effective mesh convergence (Ayturk and Puttlitz, 2011).

2.7. Validation

FE models are typically validated by comparing the FE results to *in vitro* experimental testing. This follows two commonly used methodologies, including direct and indirect validation. Direct validation involves creating the FE model to closely match the geometry, boundary and loading conditions of the experimental specimen, and directly comparing the FE results to experimental results for the same specimen. In contrast, indirect validation is when the FE model is compared to experimental results in the literature, however the model geometry, boundary and loading conditions may be different (Jones and Wilcox, 2008).

In the literature, the loading directions used for validation were identified. This search was limited to three-dimensional human lumbar FSU models, models featuring poroelastic behaviour and duplicate

model entries were removed. The results of this search can be seen in Table 1, noting that poroelastic FE models of the lumbar segments are predominantly developed for the L4-L5 FSU segments.

Although the majority of studies performed indirect validation in compression, the type of loading differed between different models. Compression was applied as a creep load over different time periods including 7.5 minutes (Velísková et al., 2018), 15 minutes (Hassan et al., 2021), 1 hour (Cheung et al., 2003), 2 hours (Argoubi and Shirazi-Adl, 1996), 8 hours (Natarajan et al., 2007) and 16 hours (Galbusera et al., 2011b). Cheung (2003) also applied sinusoidal 0.5Hz, 1Hz, 2Hz and 4Hz in compression loading. The experimental data from Heuer et al. (2007) was used by both Schmidt et al. (2007) and Zheng et al. (2022), however Schmidt et al. (2007) performed direct validation since the experiment was designed alongside the FE model whereas Zheng et al. (2022) only performed indirect validation.

Table 1: Loading directions used for validation by various FE models in the literature. The material behaviour that is used in each study is shown in the "Material Behaviour" column, where "P" represent poroelastic material behaviour and "PH" represents porohyperelastic material behaviour. For the types of validation, "I" represents indirect validation whereas "D" represents direct validation.

Study	Lumbar Segment	Material Behaviour	Compression	Anterior Shear	Posterior Shear	Left Lateral Shear	Right Lateral Shear	Left Axial Rotation	Right Axial Rotation	Left Lateral Bending	Right Lateral Bending	Flexion	Extension
Argoubi and Shirazi-Adl (1996)	L2-L3	P	I										
Hassan et al. (2021)	L3-L4	P	I										
Cheung et al. (2003)	L4-L5	P	I										
Natarajan et al. (2007)	L4-L5	P	I										
Zheng et al. (2022)	L4-L5	PH	I					I			I	I	I
Velísková et al. (2018)	L4-L5	PH	I										
Schmidt et al. (2013)	L4-L5	PH		I									
Galbusera et al. (2011b)	L4-L5	PH	I										
Schmidt et al. (2007)	L4-L5	PH										D	D

From Table 1, it can be seen that most studies perform indirect validation in limited loading directions. To the author's knowledge, no studies have performed direct validation of a lumber FSU in all 11 loading directions. Therefore, the aim of this project is to incorporate poroelastic behaviour in the L1-L2 FSU model, verify the model with results from the literature and perform direct validation of the model against experimental results in all 11 loading directions.

3. METHODOLOGY

3.1. Software

The project was undertaken on a Dell OptiPlex 3050 which had an Intel Core i5-7500, Intel HD Graphics 630 and had 8GB of RAM. The FE software Abaqus 2022 was used, with the Abaqus license provided by Flinders University. The programming languages used in this project included Python (version 3.11.4, Python Software Foundation, Wilmington, DE, USA) and MATLAB (R2022b). To manage the Python packages, Anaconda (version 2.3.1, Anaconda, Inc., Austin, TX, USA) was used with a custom environment with the relevant top-level packages including Python (version 3.11.4), numpy (version 1.25.2) and abqpy (version 2023.5.5). To create and edit code, visual studio code (version 1.81.1, Microsoft Corporation, Redmond, WA, USA) was used with extensions including abaqus (version 1.1.0), python (version 2023.14.0) and pylance (version 2023.8.40).

3.2. Original Model

The original FE model of the L1-L2 FSU was provided by Supervisor Associate Professor Paige Little as an Abaqus input file (Little and Adam, 2012). The model used the International System of Units (SI) (mm), where all dimensions and properties of the model were specified using this unit convention. The units for all dimensions included length (mm), force (N), mass (tonne), time (s), stress (MPa), density (tonne/mm^3) and specific weight (N/mm^3). All dimensions and properties used in this project were entered in the Abaqus input file using the SI (mm) units.

The author developed skills using the Abaqus Graphical User Interface, by undertaking tutorials available on the Abaqus website. The Abaqus input file of the original model was then analysed to understand all keyword, data and comment lines. Attempts were made to import the Abaqus input file into the Abaqus Graphical User Interface, however this resulted in various errors due to the limitations of the Abaqus input file reader. During this project, the model was edited in the Abaqus input file.

The nucleus was originally modelled as a fluid cavity, using hydrostatic fluid elements to line the boundary of the nucleus. The annulus was modelled as a fibre-reinforced composite structure, with the annulus bulk modelled using 8-node hexahedral elements, with embedded annulus fibres where the fibre orientation alternated $\pm 30^o$ from horizontal. The trabecular bone formed the inner region of the vertebral body modelled using 8-node hexahedral elements, whereas the cortical bone lined

the outer region and was modelled using shell elements. The original FE model of the IVD can be seen in Figure 5.

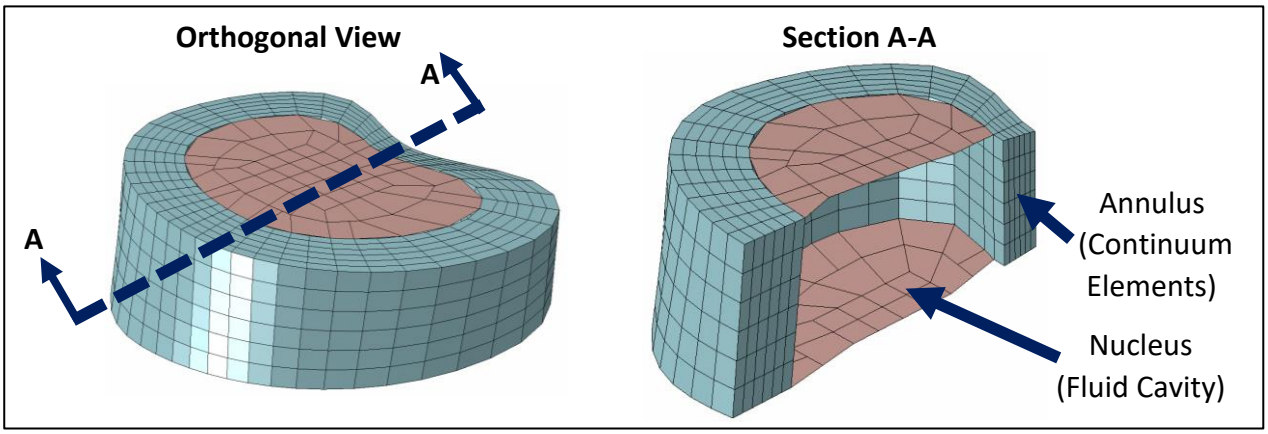

Figure 5: Original FE model of the IVD, with the section A-A taken through the mid-sagittal plane.

The facet joints were modelled using shell elements. Connector elements were used to model the ligamentum flavum, capsular ligament, supraspinous ligament and intertransverse ligament. Beam elements were used to model the interspinous ligaments, whereas spring elements were used to model the anterior longitudinal ligament and posterior longitudinal ligament. It should be noted that the model did not include the CEP and BEP. The material properties and element types used to model all tissues in the original model can be seen in Table 2.

Table 2: Material properties and element types used to model all tissues in the original model. The material properties for the nucleus include the fluid density (ρ), whereas for the annulus bulk include the coefficients of the strain energy potential equation C_{10}, C_{01} and D_1 (Little and Adam, 2012).

Tissue	Material Behaviour	Material Properties	Element Type	Element Description
Nucleus	Hydraulic (Incompressible) Fluid	$\rho = 1000\ tonne/mm^3$	F3D4	4-node hydrostatic fluid element
Annulus Bulk	Hyperelastic Mooney-Rivlin	$C_{10} = 0.7$ $C_{01} = 0.2$ $D_1 = 0.0$	C3D8H	8-node hexahedral element with full integration, hybrid formulation with constant pressure
Annulus Fibres	Elastic (No compression)	$E = 500MPa$ $v = 0.3$	SFM3D4R	4-node surface element with reduced integration
Trabecular Bone	Elastic	$E = 140MPa$ $v = 0.2$	C3D8	8-node hexahedral element with full integration
Cortical Bone	Elastic	$E = 11{,}300MPa$ $v = 0.2$	S4R	4-node shell element with reduced integration
Face Joints	Elastic	$E = 11{,}300MPa$ $v = 0.2$	S4R	4-node shell element with reduced integration
Ligamentum flavum	Nonlinear elastic		CONN3D2	2-node connector element
Capsular ligament	Nonlinear elastic		CONN3D2	2-node connector element
Supraspinous ligament	Nonlinear elastic		CONN3D2	2-node connector element
Intertransverse ligament	Nonlinear elastic		CONN3D2	2-node connector element

Tissue	Material Behaviour	Material Properties	Element Type	Element Description
Interspinous ligament	Linear elastic		B31	2-node beam element
Anterior longitudinal ligament	Nonlinear elastic		SPRINGA	2-node spring element
Posterior longitudinal ligament	Nonlinear elastic		SPRINGA	2-node spring element

The facet joints were governed using a soft exponential pressure-overclosure relationship, with the initial contact distance of 0.8mm and a contact pressure at zero distance of $p_0 = 4MPa$. Various convergence issues were encountered during this project due to the contact algorithm. After multiple unsuccessful attempts to resolve these issues by adjusting the contact properties, the contact algorithm for the facet joints was disabled. This was a significant limitation for the model, since disabling the contact at the facet joints resulted in the model not including the physiological behaviour of the facet joints, which limited the physiological relevancy of the model.

To rigidly fix the IVD to the vertebral body, tie constraints were imposed between the L1 inferior surface and IVD superior surface, as well as between the IVD inferior surface and L2 superior surface (Figure 6). A tie constraint causes all translational and rotational degrees of freedom between the two surfaces to be equal.

The experimental testing protocols for the Flinders University Hexapod robot, fixated the L1 and L2 vertebrae in cups using polymethyl methacrylate (PMMA). The L2 vertebrae was then fixed in all degrees of freedom (Amin, 2019). To simulate this in the original model, the inferior surface of the L2 vertebrae was fixed. A multiple point constraint (beam-type) was created between the L2 inferior surface and a node in the centre of the L2 vertebrae (L2 centre node), which constrained all 6 DOFs between these nodes (Figure 6). A fixed boundary condition was created on the L2 centre node during the initial step, which by extension fixed the L2 inferior surface.

The experimental testing protocols applied the loading to the L1 vertebrae (Amin, 2019). This was simulated in the original model, by applying all loading to the superior surface of the L1 vertebrae. Compression was simulated by applying a pressure load to the superior surface of the L1 vertebrae, which was a follower load which rotated with the surface during loading. To calculate the displacement of the L1 superior surface, a multiple point constraint (beam-type) was created between the L1 superior surface and a node in the centre of the L1 vertebrae (L1 centre node) (Figure 6). The displacement and rotation of the L1 centre node, was equivalent to the displacement and rotation of the entire L1 superior surface.

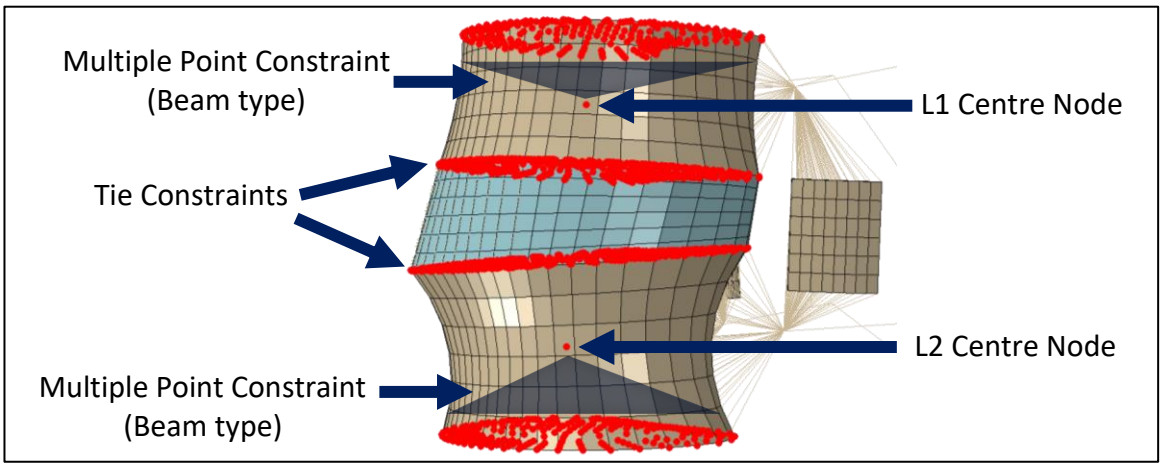

Figure 6: The different types of constraints imposed on the FE model.

3.3. Model Preparation

To ensure that the project could be completed in phases, the poroelastic properties were added in a staged manner. As per the literature review, poroelastic properties are typically assigned to the nucleus, annulus, trabecular bone, cortical bone, BEP and CEP. From Appendix B1, it can be seen that the initial voids ratio is significantly greater in the nucleus (4 to 4.88) and annulus (2.33 to 4), compared to the trabecular bone (0.4 to 1) and cortical bone (0.02 to 0.05).

Having a higher voids ratio means that the material has a greater volume of voids compared to the solid matrix, which means that the effects of the poroelastic behaviour are more significant. Therefore, poroelastic behaviour plays a bigger role in the IVD (Nucleus and annulus) compared to the vertebral bodies (Trabecular and cortical bone). Poroelastic properties were implemented in two stages, where stage 1 involved the implementation on the IVD (Nucleus and annulus) and stage 2 involved the implementation on the vertebral bodies (Trabecular and cortical bone).

Since the mesh for the original model had been created using a custom in-house code at Queensland University of Technology, changing the mesh would have required learning this custom code which would have significantly pushed back the timeline of this project. Since the focus of this project was to implement poroelastic behaviour, the original mesh was used for preliminary testing purposes. It should be noted that this decision had significant implications for the project, since it prevented the author from conducting a mesh convergence study as well as changing the element types from 8-node hexahedral elements to 20-node hexahedral elements.

As per the literature review, FE models use pore pressure elements to model the poroelastic tissues including 8-node hexahedral pore pressure elements (C3D8P) and 20-node hexahedral pore pressure elements (C3D20P). The original model used regular 8-node hexahedral elements to model the

tissues. Since the original mesh was not changed during this project, 8-node hexahedral pore pressure elements were used in the implementation of poroelastic behaviour.

As per the Abaqus documentation, pore pressure elements cannot be used in the same model as hydrostatic fluid elements (Dassault Systèmes., 2022e). Since the nucleus was modelled as a fluid cavity using hydrostatic fluid elements, the nucleus elements were changed from hydrostatic fluid elements to continuum elements. The original node set for the IVD, had nodes defined in the entire IVD volume including within the nucleus cavity (Figure 7).

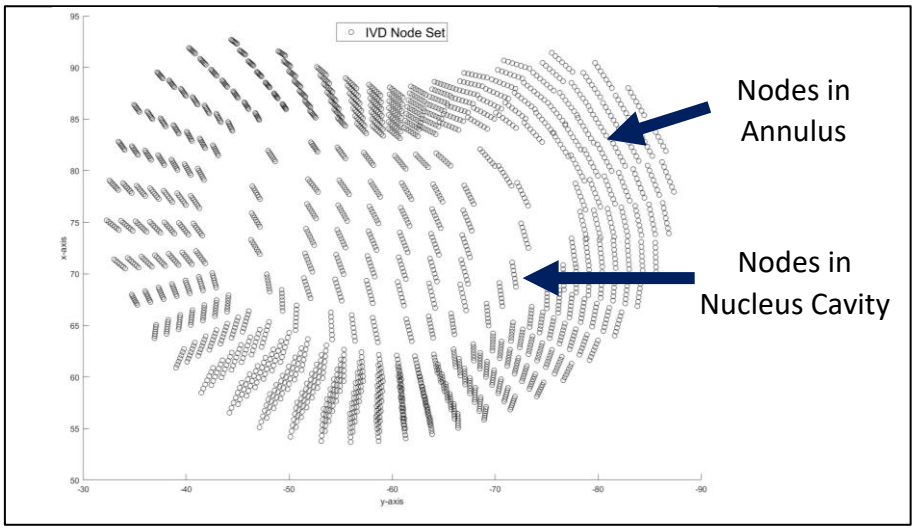

Figure 7: Original node set for the IVD, where nodes are defined within the annulus and nucleus cavity.

To eliminate the need to create a new mesh for the model, the nucleus elements were created using the nodes defined in the original node set for the IVD. The elements defined in the nucleus were 8-node hexahedral elements. A MATLAB script was created, to define the element connectivity matrix for the nucleus elements (Appendix C). The first step in the MATLAB script, involved importing the relevant node sets and elements sets from the original model as separate text files. This included the node set for the IVD, as well as the element sets for the annulus bulk and nucleus fluid cavity. Node sets for the annulus and nucleus were then created (Figure 8).

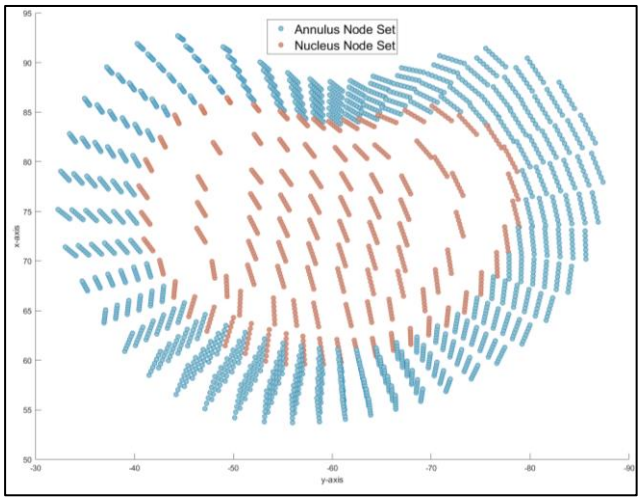

Figure 8: Node sets created for the nucleus and annulus.

To create the element connectivity matrix for the nucleus elements, the naming convention for all nodes in the nucleus node set was studied. As seen in Figure 9, the node set for the nucleus had seven layers (Bottom layer to top layer) where each layer had the same layout of nodes. Therefore, if the element shape could be established on one layer, this could be connected to the same nodes in the layers above and below. The bottom layer was used to create the element shape.

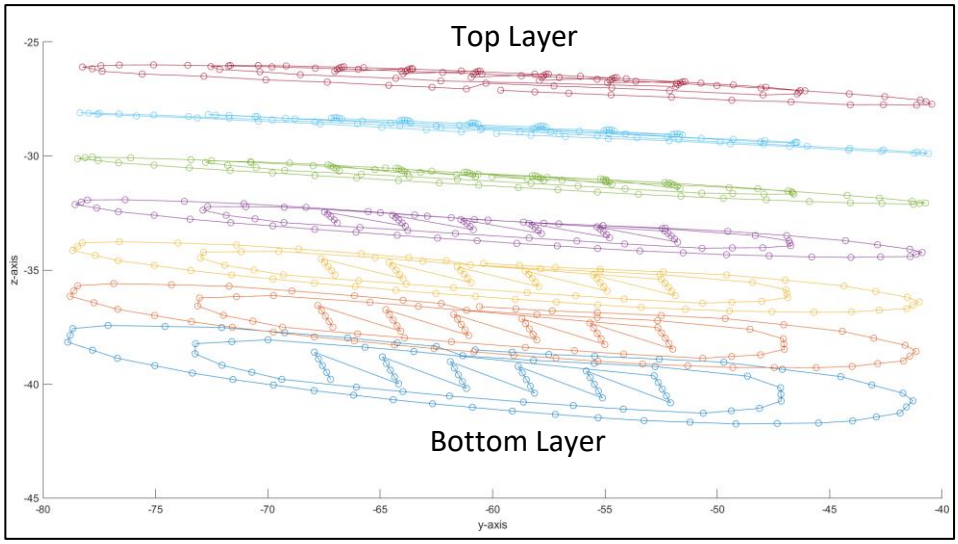

Figure 9: Node set for the nucleus, which had 7 horizontal layers with each layer having the same layout of nodes.

A cross-sectional view of the bottom layer in Figure 10(a), was used to develop the shape of the nucleus elements. The element shape was created manually in Figure 10(b), where the angle of each side was kept as close to 90^{o} as possible. However, due to the small number of nodes, various elements had poor shape as highlighted in Figure 10(b).

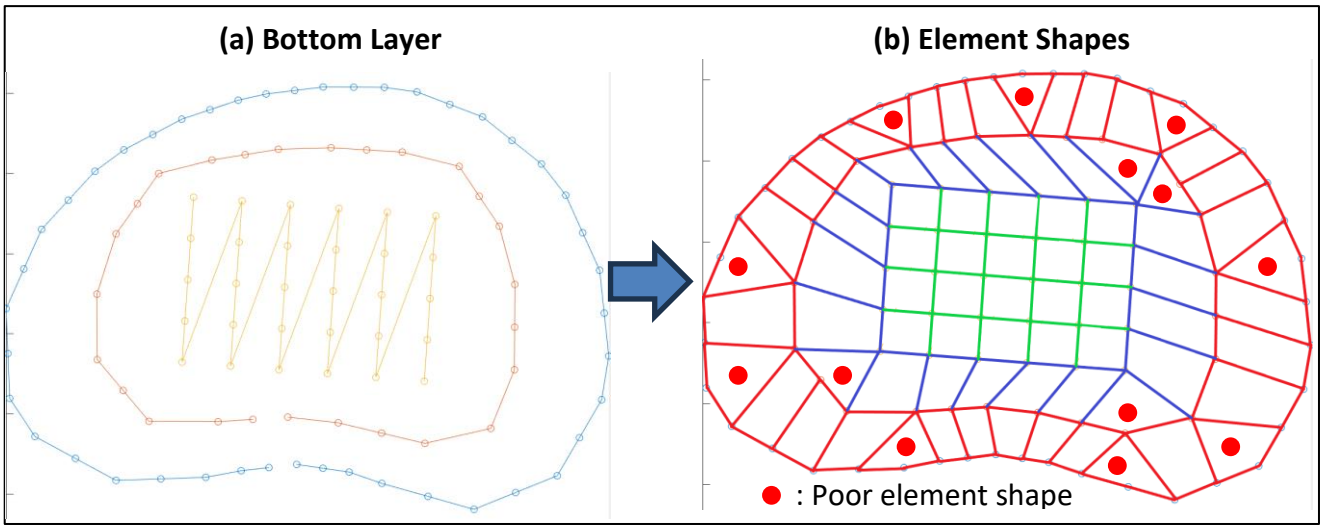

Figure 10: (a) Cross-sectional view of the bottom layer. (b) Element shapes created manually, where elements with a poor shape are highlighted with a red circle.

Using the two-dimensional element shape established in Figure 10(b), the element connectivity matrix for 8-node hexahedral elements was then created. Each node was connected to the corresponding nodes on the layers above and below. The nucleus node set, annulus node set, and nucleus element set were then exported as text files and copied into the Abaqus input file. The final IVD model with the nucleus 8-node hexahedral elements is shown in Figure 11.

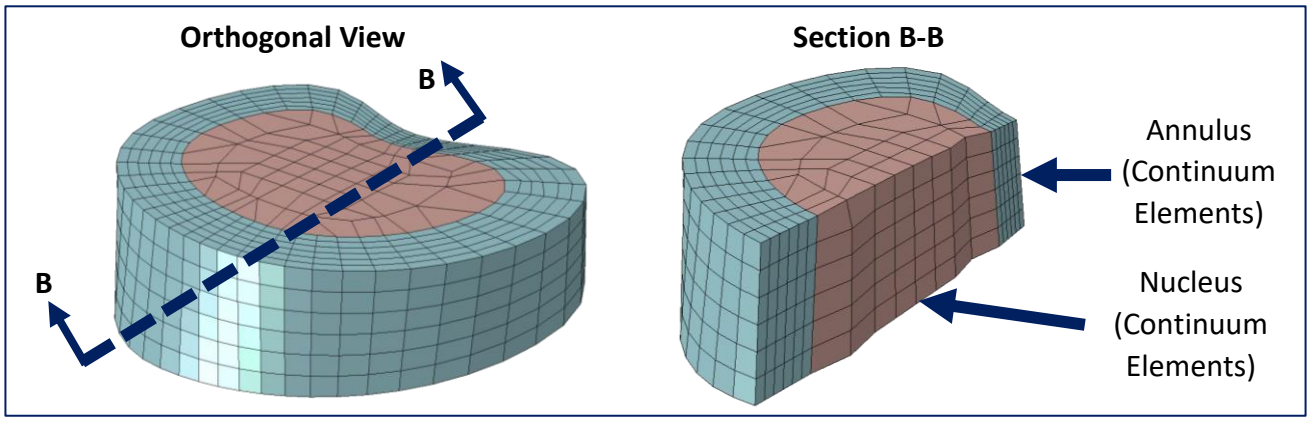

Figure 11: Final FE model of the IVD, with the section B-B taken through the mid-sagittal plane.

3.4. Poroelastic Behaviour Implementation

The nucleus and annulus bulk were assigned poroelastic properties, whereas the annulus fibres, trabecular bone and cortical bone were assigned elastic properties. To simplify the implementation of poroelastic behaviour, the solid phase of the poroelastic tissues was assumed to have elastic material properties, and the permeability was assumed to be constant. The material properties that were defined for the poroelastic tissues included the elastic modulus, poisson's ratio, specific permeability (k_s), initial voids ratio (e_o) and specific weight of the interstitial fluid (γ_w). It should be noted that the material density did not affect the results.

Very few studies in the literature reported the specific weight used to model poroelastic tissues, other than a study by Silva et al. (2005) which assumed a specific weight equivalent to water ($\gamma_w = 9965N.m^{-3}$). In the literature, the absolute permeability k (units: $m^4.N^{-1}.s^{-1}$) was provided, however Abaqus required the specific permeability k_s (units: $mm.s^{-1}$) which was found using equation (6) (Silva et al., 2005).

$$k_s(\mathrm{mm.s^{-1}}) = k(\mathrm{m^4.N^{-1}.s^{-1}}) \times \gamma_w(N.m^{-3}) \times \frac{1000mm}{1m} \qquad 6$$

The material properties for the nucleus, annulus bulk, annulus fibres, trabecular bone and cortical bone were derived from a study by Ferguson et al. (2004). The elements used to model the nucleus and annulus bulk, were then changed from regular 8-node hexahedral elements (C3D8) to pore

pressure 8-node hexahedral elements (C3D8P). The material properties and element types used to model all tissues in the final model can be seen in Table 3.

Table 3: Material properties and element types, used to model all tissues in the final model. The absolute permeability for both the nucleus and annulus was specified as k = 7.5E-16 m^4/Ns and this was used to calculate the specific permeability as shown in the table. The elastic modulus, poisson's ratio, absolute permeability and initial voids ratio were derived from Ferguson et al. (2004), whereas the specific weight was derived from Silva et al. (2005).

Tissue	Material Behaviour	Elastic Modulus E (MPa)	Poisson's Ratio v	Specific Permeability k_s $(mm.s^{-1})$	Initial Voids Ratio e_o	Specific Weight γ_w $(N.mm^{-3})$	Element Type	Element Description
Nucleus	Poroelastic	1.5	0.17	7.4738E-09	4	9.965E-06	C3D8P	8-node hexahedral element with trilinear interpolation of displacement and pore pressure
Annulus Bulk	Poroelastic	2.5	0.17	7.4738E-09	2.33	9.965E-06	C3D8P	8-node hexahedral element with trilinear interpolation of displacement and pore pressure
Annulus Fibres	Elastic	60	0.33				SFM3D4R	4-node surface element with reduced integration
Trabecular Bone	Elastic	100	0.20				C3D8	8-node hexahedral element with full integration
Cortical Bone	Elastic	10,000	0.30				S4R	4-node shell element with reduced integration
Facet Joints and Ligaments	Same as the original model in Table 2. Note that the contact algorithm for the facet joints was disabled, due to convergence issues.							

During the initial step in Abaqus, initial conditions were created to assign the initial voids ratio to the nucleus node set and annulus node set as per Table 3. Although pore pressure elements can be used in either a soils analysis or geostatic analysis (Dassault Systèmes., 2022e), studies in the literature simulate poroelastic behaviour using soils analysis with transient pore fluid response (Silva et al., 2005; Hassan et al., 2021). Therefore, the loading step was changed from a Static step to a Soils step, with the pore fluid response being governed using transient behaviour.

With the displacement of the model being relatively large, the non-linear geometry option was turned on to account for geometric nonlinearities (Dassault Systèmes., 2022f). The option for including the effects of creep, swelling or viscoelasticity was enabled since this model would simulate swelling. The loading step used automatic time incrementation, where the initial increment size was set to 0.01 seconds, minimum increment size to 10^{-6} seconds, maximum increment size to 60 seconds and maximum number of increments was set to 2000. The maximum pore pressure change that was allowed in an increment before the analysis terminated was set to 10^6MPa.

3.5. Boundary and Loading Conditions

Within the model, the boundary conditions and loads were applied using a custom amplitude curve. Amplitude curves allowed the variation of the load magnitude over time in each loading step, and were defined in tabular form. The custom amplitude curves used in this project included a step input, ramp input over 1 second and ramp input over 10 seconds. To remove the load at the end of the loading step over 1 or 10 seconds, a ramp input with a negative slope was used in the last 1 or 10 seconds of the loading step.

The experimental testing protocols were then simulated in the FE model (Figure 12). In the experiment, the L1 and L2 vertebrae were fixated in cups using PMMA. The experimental testing protocols included fixing the L2 vertebrae, applying a 12-hour axial compressive preload on the L1 vertebrae to simulate a nucleus pressure of 0.1MPa, and applying all experimental loads on the L1 vertebrae.

The experimental testing protocols were simulated in the FE model, by assigning a fixed support boundary condition on the inferior surface of the L2 vertebrae. The axial compressive load was applied to the superior surface of the L1 vertebrae as a pressure load, where the pressure was obtained by dividing the applied force by the surface area of the superior surface of the L1 vertebrae (Equation (7)). Applying the boundary and loading conditions to the superior surface of the L1 vertebrae and inferior surface of the L2 vertebrae, was consistent with the literature (Argoubi and Shirazi-Adl, 1996; Cheung et al., 2003).

$$p = \frac{F}{A_{Superior\ Surface\_L1\ Vertebrae}} = \frac{F}{1257.65mm^2} \quad 7$$

As seen in the literature review, various models are used to simulate the osmotic behaviour of the IVD including the boundary pore pressure, FOP, FOP-N and BS models. The boundary pore pressure model could be implemented using the default definition fields available in Abaqus whereas the FOP, FOP-N and BS models all required the use of user subroutines. The boundary pore pressure model was found to produce acceptable approximations for simulating the osmotic behaviour of the IVD (Galbusera et al., 2011c). Due to its ease of implementation, the boundary pore pressure model was implemented in this project.

The boundary pore pressure model prescribed a boundary condition where a fixed pore pressure was assigned to the nodes, which forced fluid to enter and leave the nodes to maintain this pore pressure (Dassault Systèmes., 2022g). As per the literature review, the boundary pore pressure was assigned

either to the boundary of the IVD, or to all external surfaces of the IVD and vertebral bodies. Since only the IVD was modelled using poroelastic behaviour, the boundary pore pressure was assigned to the boundary of the IVD. A node set for the IVD boundary was created using the MATLAB script in Appendix C, and this node set was copied into the Abaqus input file. A pore pressure boundary condition of 0.1MPa was implemented on the IVD boundary, and this was applied in the first loading step as a step input (Figure 12).

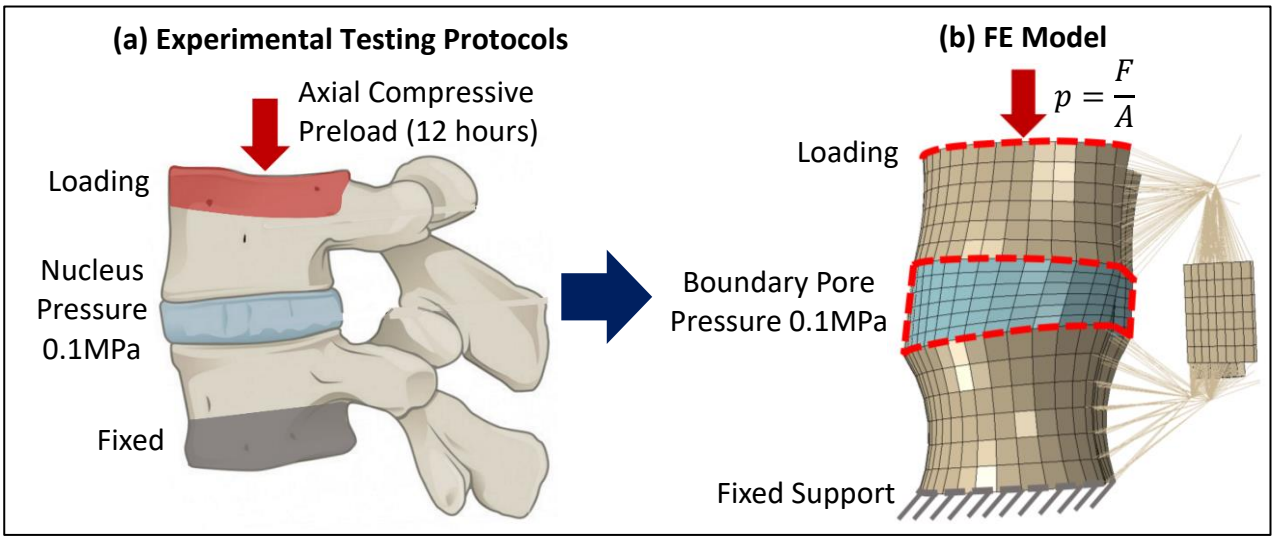

Figure 12: Boundary and loading conditions of the (a) Experimental testing protocols and (b) FE model. The image in (a) was adapted from Asaad et al. (2020), reused under a Creative Commons Attribution license.

3.6. Outputs

The outputs were obtained at specific nodes in Figure 13, which were based on the outputs used in the literature. These included the centre of the IVD superior surface (Node A), centre of the IVD inferior surface (Node B), centre of the nucleus (Node C), inner anterior annulus (Node D), outer anterior annulus (Node E) and lateral annulus (Node F). Nodes A and B were based on Cheung et al. (2003), whereas nodes C, D, E and F were based on Malandrino et al. (2009). The coordinate system used in this project can be seen in Figure 13.

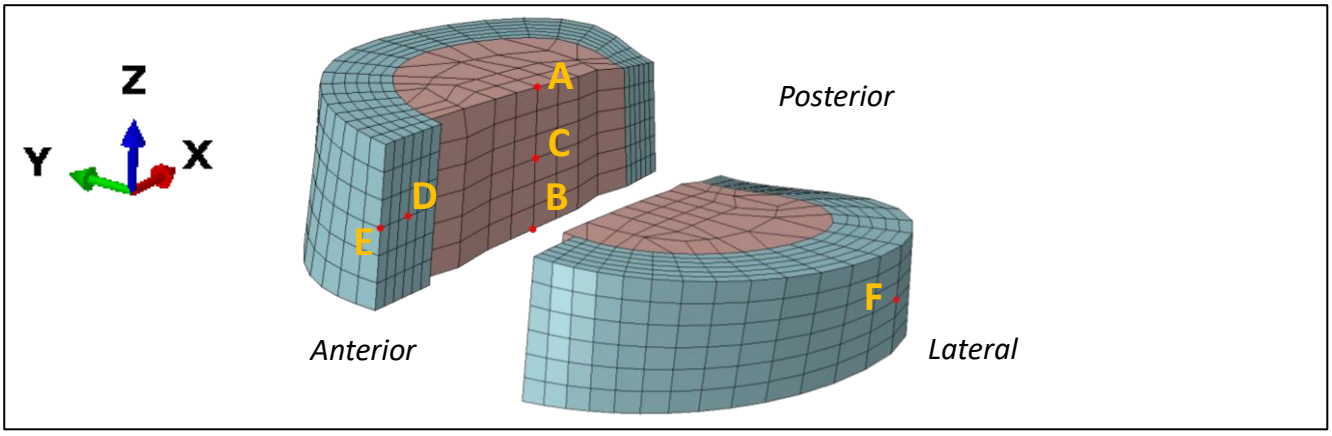

Figure 13: Location of the outputs used in this project. A: Centre of IVD superior surface. B: Centre of IVD inferior surface. C: Centre of nucleus. D: Inner anterior annulus. E: Outer anterior annulus. F: Lateral annulus.

The IVD height was calculated as the vertical distance between the centre of the IVD superior surface (Node A) and centre of the IVD inferior surface (Node B) (Cheung et al., 2003). The change in IVD height was then found, by calculating the relative vertical displacement between nodes A and B (Equation (8)).

$$\Delta\, IVD\ Height = u_{z\_NodeA} - u_{z\_NodeB} \tag{8}$$

The volume of all elements in the nucleus and annulus were specified as an output, and these were summated to obtain the total volume of the nucleus and annulus. The change in volume of the nucleus and annulus was calculated, by finding the percentage difference between the current volume and the initial volume prior to loading (Equation (9)).

$$Change\ in\ Volume = \frac{V_{current} - V_{initial}}{V_{initial}} \times 100\ \% \tag{9}$$

3.7. Post-Processing

To automate the running of simulations and extraction of results, two python scripts were created including a Batch script and Data Extraction script in Appendix D (Figure 14). The Batch script submitted the Abaqus input file to the Abaqus Standard solver, which produced an Abaqus Output Database file. The Batch script then called the Data Extraction script, which opened the Abaqus Output Database file and extracted all of the relevant outputs. These outputs were then exported as a Microsoft Excel spreadsheet, to allow for further data analysis. This scripting significantly reduced the post-processing time associated with the project.

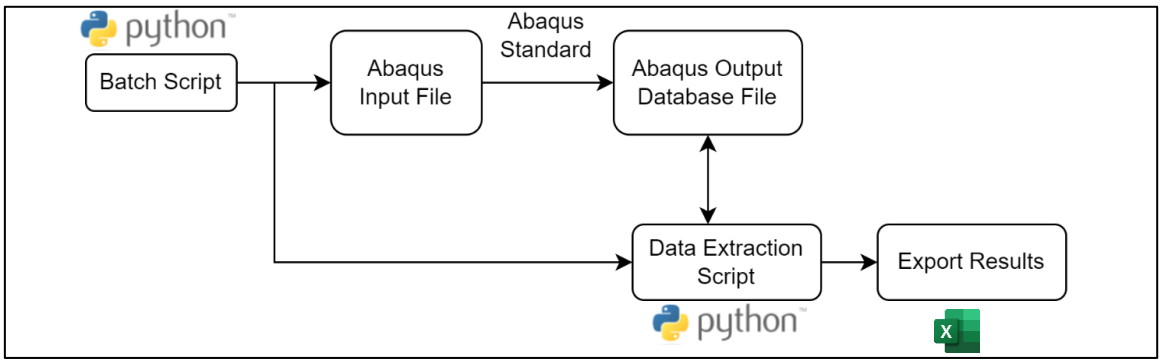

Figure 14: Flow chart for the scripting used to post-process the Abaqus results.

4. VERIFICATION

The implementation of poroelastic behaviour was then verified, by comparing the results against three different studies in the literature where each study focused on different aspects of the model including the osmotic behaviour, loading behaviour and pore pressure distribution. For each study in the literature, the boundary and loading conditions were replicated in the final model. Since various studies modelled the IVD using hyperelastic behaviour, the material properties of the studies in the literature were not replicated in the final model. The results from the final model were then compared against the results published in each study.

4.1. Study 1: Galbusera

4.1.1. Methodology

Studies typically have an initial free swelling period, where no loads are applied which allows the IVD to swell. This swelling period ranges from 8 hours (Galbusera et al., 2011c; Schmidt et al., 2011) to 24 hours (Galbusera et al., 2011a). To investigate the swelling behaviour of the final model, verification was conducted on a study by Galbusera et al. (2011c). The model developed by Galbusera et al. (2011c), consisted of a L4-L5 FSU which included the vertebrae, IVD, posterior elements and seven major ligaments.

The poroelastic properties were assigned to the nucleus, annulus bulk, CEP, trabecular bone and cortical bone. For the poroelastic tissues, the solid phase of the nucleus and annulus bulk was defined using hyperelastic behaviour, whereas the solid phase of the remaining tissues were defined using elastic behaviour. Strain-dependent permeability was defined for the nucleus, annulus bulk and CEP. The model by Galbusera et al. (2011c), assigned a boundary pore pressure of 0.165MPa on all external surfaces of the IVD and vertebral bodies. Since only the IVD was modelled using poroelastic behaviour, this was replicated in the final model with a boundary pore pressure of 0.165MPa on the boundary of the IVD.

4.1.2. Results

The results used in this verification study included the pore pressure in the centre of the nucleus (Figure 15), change in volume of the nucleus and annulus (Figure 16), axial displacement of the centre of the IVD superior surface (Figure 17) and the lateral displacement of the most lateral point of the IVD (Figure 18).

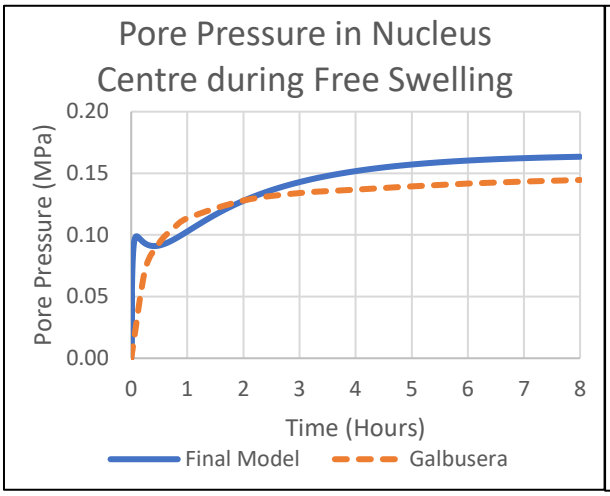

Figure 15: Pore pressure in the centre of the nucleus during the 8 hours of free swelling. Results approximated from Galbusera et al. (2011c).

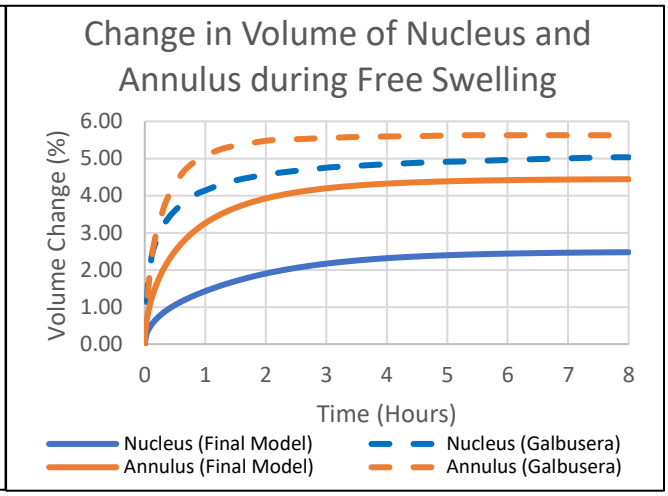

Figure 16: Change in volume of the nucleus and annulus relative to the initial state, during the 8 hours of free swelling. Results approximated from Galbusera et al. (2011c).

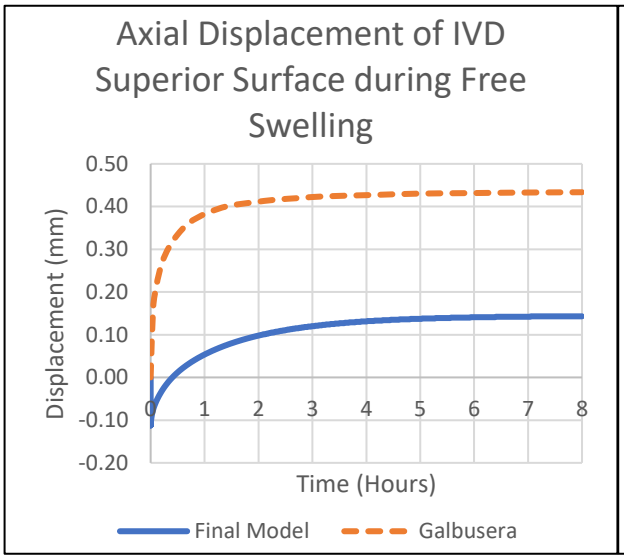

Figure 17: Axial (z) displacement of the centre of the IVD superior surface during the 8 hours of free swelling. Note that positive displacement represents movement superiorly. Results approximated from Galbusera et al. (2011c).

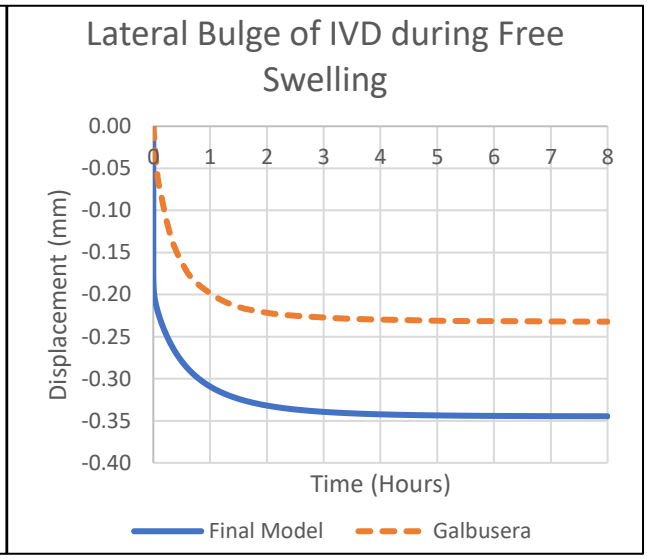

Figure 18: Lateral (y) displacement of the lateral annulus during the 8 hours of free swelling. Note that negative displacement represents movement laterally. Results approximated from Galbusera et al. (2011c).

Steady state was achieved, when the current value was within 0.5% of the final value. As seen in Figure 15, the pore pressure in the centre of the nucleus for the final model had an initial peak of 0.1MPa, followed by a gradual increase to a final value of 0.163MPa at the end of the free swelling period. Galbusera's model increased exponentially, reaching a final value of 0.145MPa at the end of the free swelling period. The final model reached steady state after approximately 7.2 hours, whereas Galbusera's model did not reach steady state.

During the 8-hours of free swelling, the volume of the nucleus and annulus both increased (Figure 16). At the end of the free swelling period for the final model, the volume of the nucleus increased by 2.5% and annulus increased by 4.4%. This volume increase was less than Galbusera's model, where

the volume of the nucleus increased by 5% (50% higher than final model) and annulus increased by 5.6% (21% higher than final model).

As seen in Figure 17, the axial displacement of the IVD superior surface for the final model, instantaneously decreased to -0.11mm at the start of loading and gradually increased to a final value of 0.14mm. The axial displacement of Galbusera's model increased gradually, reaching a final value of 0.43mm (67% higher than final model). From Figure 18, the lateral displacement of the most lateral point of the IVD instantaneously decreased to -0.18mm followed by a gradual decrease to -0.35mm after 8 hours. The lateral displacement of Galbusera's model decreased gradually reaching a final value of -0.23mm (52% lower than final model).

4.1.3. Discussion

The boundary pore pressure prescribed on the boundary of the IVD, forced the flow of fluid through the IVD boundary to maintain this pore pressure. The boundary pore pressure of 0.165MPa promoted the flow of fluid into the IVD, which could be seen in the results where the volume of the nucleus and annulus increased during the 8-hours of free swelling. Over time, the pore pressure in the centre of the nucleus equilibrated with the boundary pore pressure prescribed on the boundary of the IVD.

The pore pressure in the centre of the nucleus equilibrated with the boundary pore pressure significantly faster in the final model, compared to Galbusera et al. (2011c) which did not reach equilibrium within the 8 hours of free swelling. However, the same author has conducted other studies using the boundary pore pressure method where free swelling was conducted over 24 hours, to ensure that the pore pressure in the centre of the nucleus equilibrated with the boundary pore pressure (Galbusera et al., 2011a, 2011b).

The decreased time taken to reach pore pressure equilibration, was likely due to the differences in the boundary conditions between the final model and Galbusera et al. (2011c). The final model assigned the boundary pore pressure to the boundary of the IVD, whereas Galbusera et al. (2011c) assigned the boundary pore pressure to all external surfaces of the IVD and vertebral bodies. Since Galbusera et al. (2011c) also assigned poroelastic properties to the vertebral bodies, the fluid had to flow through the vertebral bodies as well as the IVD which increased the time taken for the pore pressure in the centre of the nucleus to equilibrate with the boundary pore pressure.

The pore pressure in the centre of the nucleus for the final model had an initial peak, which was not seen in the results from Galbusera et al. (2011c). It should also be noted that at the start of loading,

the axial displacement of the IVD superior surface and lateral bulge of the IVD instantaneously increased in magnitude. The instantaneous changes in displacement at the start of loading, likely caused the pore pressure to increase to a peak value. This suggests that the initial state of the final model was not stable, since the model needed to undergo instantaneous displacement to reach a stable state.

In the final model, the boundary pore pressure was applied as a step input during the first loading step. The method used to apply the boundary pore pressure was not published by Galbusera et al. (2011c), which may have been applied using a different type of input (e.g. ramp input) over the first loading step. The pore pressure increasing to a peak value in the final model, may also be due to the boundary pore pressure being applied as a step input.

The 8-hours of free swelling, resulted in the increase in the volume of the nucleus and annulus as fluid flowed into the IVD. However, the volume increase was considerably lower in the final model compared to Galbusera et al. (2011c) for both the nucleus (50% lower) and annulus (21% lower). Since the nucleus elements were created during this project, a mesh convergence study was unable to be carried out due to the time constraints. The differences in the volume change for the nucleus between the final model and Galbusera et al. (2011c), may be due to a poorly converged mesh.

The increase in the volume of the nucleus and annulus during the 8-hours of free swelling, also resulted in the IVD superior surface moving superiorly. The most lateral point of the IVD was displaced laterally, which resulted in the bulging of the IVD. Comparing the final model with Galbusera et al. (2011c), it can be seen that the final model had a smaller axial displacement of the IVD superior surface (67% lower) while having greater lateral bulging (52% greater).

Since the volume of the nucleus increased 50% less in the final model compared to Galbusera et al. (2011c), this resulted in the IVD superior surface having decreased axial displacement. In the final model, the volume of the nucleus increased less than the annulus, which means that although the increased annulus volume induced axial displacement, this was resisted by the smaller increase in nucleus volume. Although various discrepancies were present between the final model and Galbusera et al. (2011c), this can be attributed to the final model using a simplified implementation of poroelastic behaviour as well as a poorly converged mesh.

4.2. Study 2: Ferguson

4.2.1. Methodology

To verify the loading behaviour of the final model, verification was conducted against a study by Ferguson et al. (2004). The model developed by Ferguson et al. (2004), was an axisymmetric FE model of a generic lumbar FSU segment consisting of the vertebrae and the IVD, however it did not include the posterior elements and ligaments. The poroelastic properties were assigned to the nucleus, annulus bulk, CEP, cortical bone and trabecular bone. For all poroelastic tissues, the solid phase was defined using elastic behaviour. The permeability was strain-dependent for the nucleus, annulus bulk and CEP. Although the study also analysed a mass transport model which defined the flow of solutes through the IVD, this was separate to the poroelastic study.

The model by Ferguson et al. (2004) assigned a boundary pore pressure of 0.2MPa on the boundary of the IVD, which was replicated in the final model. Ferguson et al. (2004) simulated 2 daily loading cycles, with each day consisting of 8 hours of rest and 16 hours of loading. An axial compressive load was applied on the superior surface of the superior vertebrae, which was 0MPa during rest and 0.5MPa during loading. The loading was applied and removed using step inputs. Two daily loading cycles were simulated in the final model, where the axial compressive load was applied as a ramp input over 1 second which was assumed to be equivalent to the step inputs used by Ferguson et al. (2004) (Figure 19).

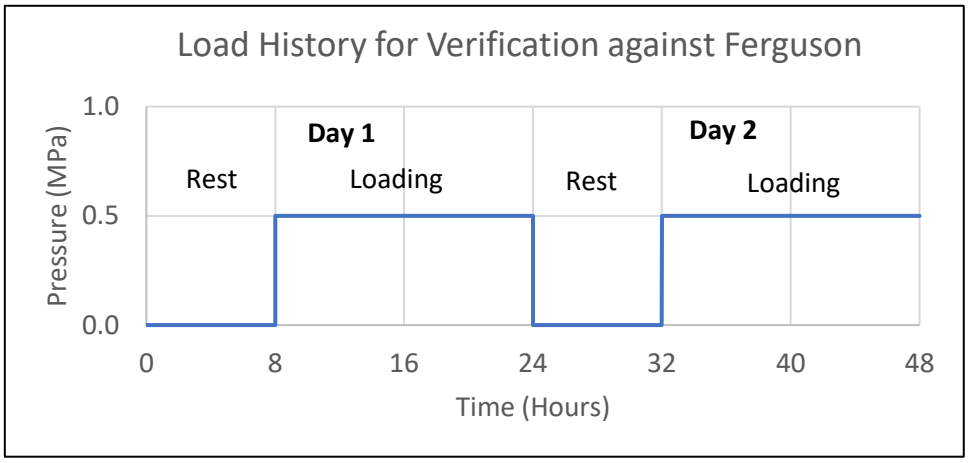

Figure 19: Load history of the axial compressive load applied to the superior surface of the L1 vertebrae, during the verification against Ferguson et al. (2004).

4.2.2. Results

The results were analysed during Day 2 of the daily loading cycle which was between 24 to 48 hours, which was consistent with the results used by Ferguson et al. (2004). Prior to loading, the initial IVD height for the final model was 13.3mm, whereas for Ferguson's model was 12.5mm. As the load was applied and removed, the change in IVD height was found using equation (8). The rest period where no loads are applied, is where fluid was allowed to imbibe the tissues causing them to swell resulting in an increase in IVD height. At the end of the rest period, the IVD height was at its maximal value. The change in IVD height was normalised with respect to the end of the Day 2 Rest period, which allowed for the comparison of the results against the maximal IVD height value. The change in IVD height over Day 2, was then compared against the results published by Ferguson et al. (2004) in Figure 20.

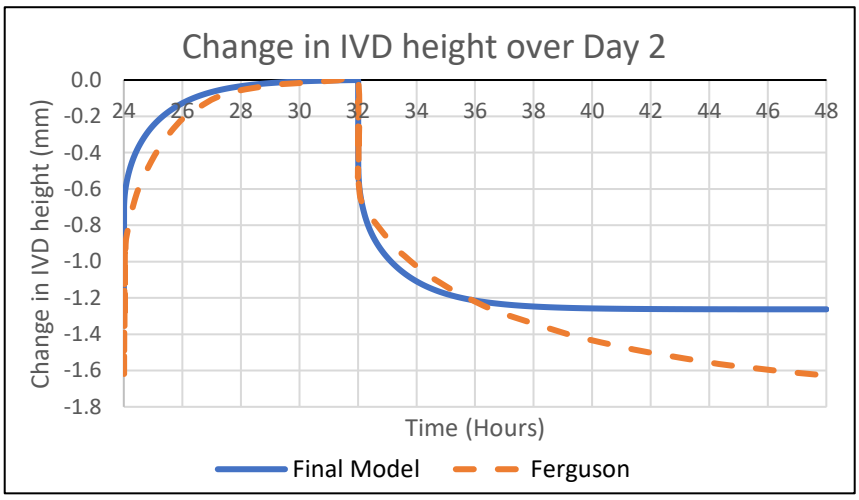

Figure 20: Change in IVD height over Day 2. Note that the change in IVD height has been normalised with respect to the end of the Day 2 Rest period (At 32 hours). Results approximated from Ferguson et al. (2004).

From Figure 20, at the start of the Day 2 Rest period (24 to 32 hours), the IVD started in a compressed state from the previous loading step (Day 1 Loading period). Relative to the maximal IVD height, the change in IVD height at 24 hours for the final model was -1.25mm whereas Ferguson's model was -1.6mm. As the load was removed during the Day 2 Rest period, the IVD height increased to the maximal IVD height.

The Day 2 Loading period (32 to 48 hours) caused the IVD height to decrease. Immediately after load application, the IVD height for the final model decreased by 0.5mm whereas Ferguson's model decreased by 0.55mm. The IVD height for the final model reached a steady state after 7.6 hours that was -1.25mm less than the maximal IVD height, whereas Ferguson's model did not reach steady state reaching -1.6mm at the end of the Day 2 Loading period. The Day 2 Loading period caused the final model to decrease by 9.5% of the initial IVD height, whereas Ferguson's model decreased by 12% of the initial IVD height.

4.2.3. Discussion

The results showed that the IVD height lost during the 16 hours of axial compressive loading, was completely recovered during the 8 hours of rest. The total change in IVD height due to the axial compressive loading, was lower in the final model (9.5% of initial IVD height) compared to Ferguson et al. (2004) (12% of initial IVD height). This difference in the change in IVD height may have been due to the differences in geometry between the models, since Ferguson et al. (2004) did not model the posterior elements and ligaments whereas the final model included the full FSU.

The final model assigned poroelastic properties to the nucleus and annulus bulk, whereas Ferguson et al. (2004) assigned poroelastic properties to the nucleus, annulus bulk, cortical and trabecular bone. Since the final model did not incorporate poroelastic properties on the vertebral bodies, fluid was not able to flow through the vertebral endplates. The pathway of fluid flow has been found to be dominant through the vertebral endplates compared to the annulus periphery (Schmidt and Shirazi-Adl, 2018). Obstructing the flow of fluid through the vertebral endplates, was found to decrease the fluid expression which caused a decreased change in IVD height (Ferguson et al., 2004). Since the final model had a decreased change in IVD height compared to Ferguson et al. (2004), this may also have been due to the final model not defining poroelastic properties for the vertebral bodies, which prevented fluid from flowing through the vertebral endplates.

During the Day 2 Loading period, the change in IVD height of the final model achieved steady state whereas Ferguson et al. (2004) did not reach steady state. It should be noted that the final model assigned a constant permeability for the nucleus and annulus bulk, whereas Ferguson et al. (2004) assigned a strain-dependent permeability for the nucleus and annulus bulk. The strain-dependent permeability was governed using equation (3), where the permeability decreased as the compressive strain increased (Ferguson et al., 2004). This decreased permeability, increased the resistance to fluid flow which increased the stiffness of the response (Argoubi and Shirazi-Adl, 1996). As the axial compressive load was applied, the compressive strain on the IVD increased, resulting in a decreased permeability which increased the resistance to further fluid flow. The gradual change in the IVD height in Ferguson et al. (2004), may also have been due to the presence of strain-dependent permeability. These results showed various differences between the final model and Ferguson et al. (2004), however these can be attributed to the differences in the geometry, material properties and tissue permeability.

4.3. Study 3: Schmidt

4.3.1. Methodology

During periods of unloading where the axial compressive load was removed, the poroelastic constitutive equations predict a negative pore pressure in the IVD. However, this negative pore pressure does not exist *in vivo*, and is therefore fictional in nature (Schmidt et al., 2011). A study by Schmidt et al. (2011) investigated the causes and techniques for avoiding negative pore pressures, where a contour plot of the pore pressure distribution was reported at various time periods during the loading cycle. To investigate the pore pressure distribution in the final model, verification was conducted against the study by Schmidt et al. (2011).

Schmidt et al. (2011) modelled the L4-L5 FSU which included the vertebrae, IVD, posterior elements and seven major ligaments. The nucleus, annulus bulk, CEP, BEP, trabecular bone and cortical bone were modelled using poroelastic material properties. The solid phase of the nucleus and annulus bulk was modelled using hyperelastic behaviour, whereas the solid phase of the trabecular and cortical bone was modelled using elastic behaviour. Strain-dependent permeability was defined for all poroelastic tissues.

The model by Schmidt et al. (2011), assigned a boundary pore pressure of 0MPa on all external surfaces of the IVD and vertebral bodies. This was replicated in the final model, with a boundary pore pressure of 0MPa applied on the boundary of the IVD. Two daily loading cycles were simulated, in which each day consisted of 8 hours of rest and 16 hours of loading. The axial compressive load was applied to the superior surface of the L1 vertebrae, which was 0N during rest and 1000N during loading (Figure 21). This force was converted to a pressure load using equation (7). All loads were applied and removed over 10 seconds, which was consistent with Schmidt et al. (2011).

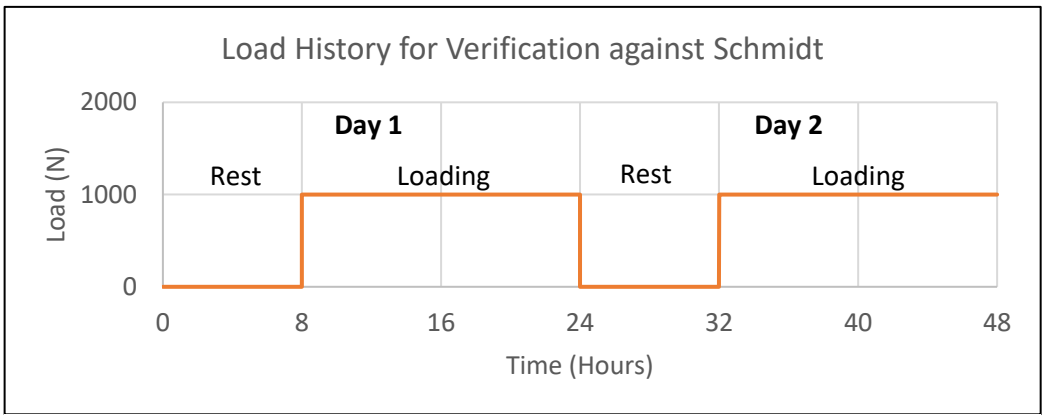

Figure 21: Load history for the axial compressive load applied to the superior surface of the L1 vertebrae, replicating the loading conditions of Schmidt et al. (2011).

4.3.2. Results

The contour plots for the pore pressure distribution, were obtained at the same time periods as that obtained by Schmidt et al. (2011) to allow for comparison (Figure 22). The pore pressure was also obtained along a path of nodes in the vertical direction (Shown in Figure 22), where the pore pressure was plotted against the vertical height from the centre of the IVD inferior surface in Figure 23. Various outputs were obtained from the model, including the pore pressure in the centre of the nucleus during Day 2 (Figure 24), the axial displacement of the centre of the nucleus during the Day 2 Rest period (Figure 25) and Day 2 Loading period (Figure 26), noting that the displacements were zeroed at the start of each period to highlight the change in displacement.

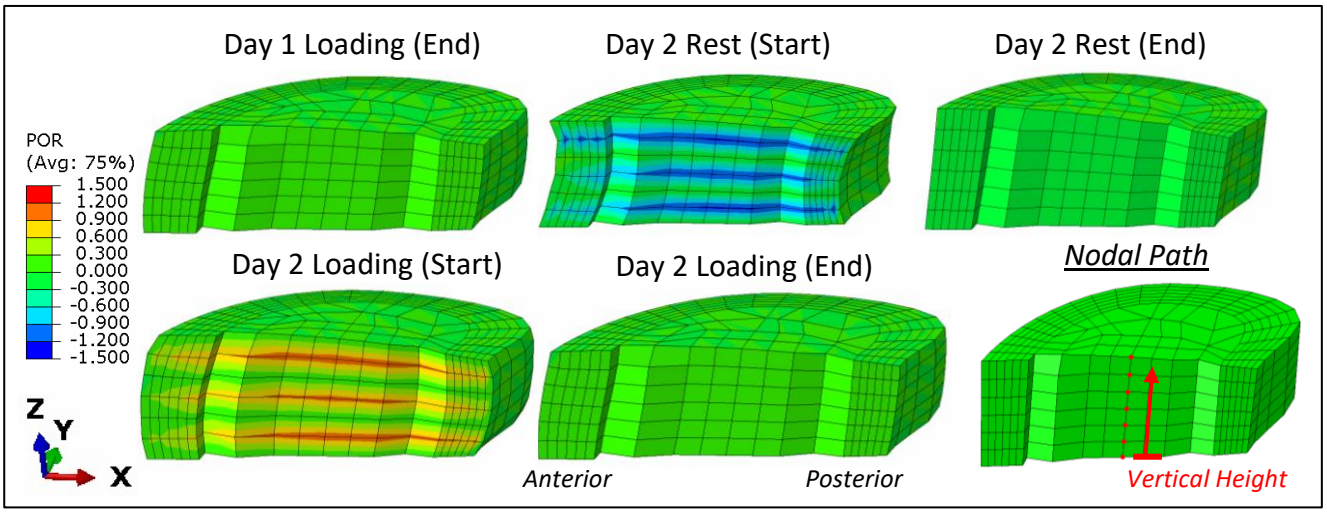

Figure 22: Contour plots for the pore pressure distribution of the final model. The path of nodes used to obtain the outputs of pore pressure can be seen in the bottom right, with the results shown in Figure 23.

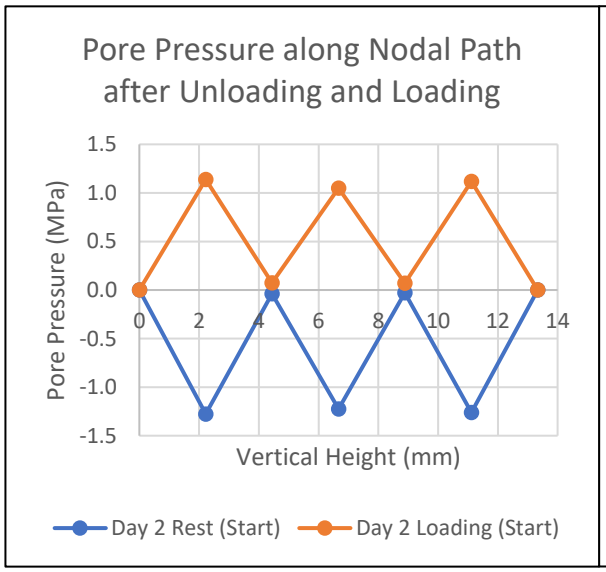

Figure 23: Pore pressure obtained along a path of nodes as shown in Figure 22, where the vertical height is from the centre of the IVD inferior surface. This is obtained at the start of the Day 2 Rest (Immediately after unloading) and start of Day 2 Loading (immediately after loading).

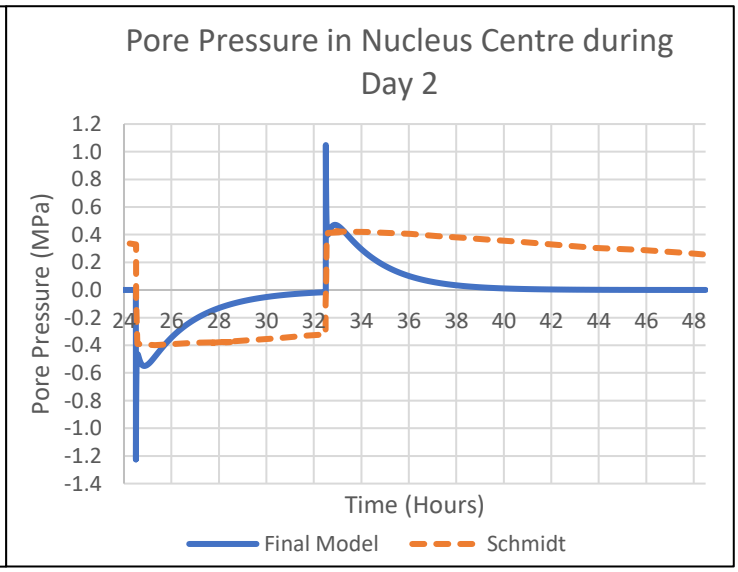

Figure 24: Pore pressure in the centre of the nucleus during Day 2. Results approximated from Schmidt et al. (2011).

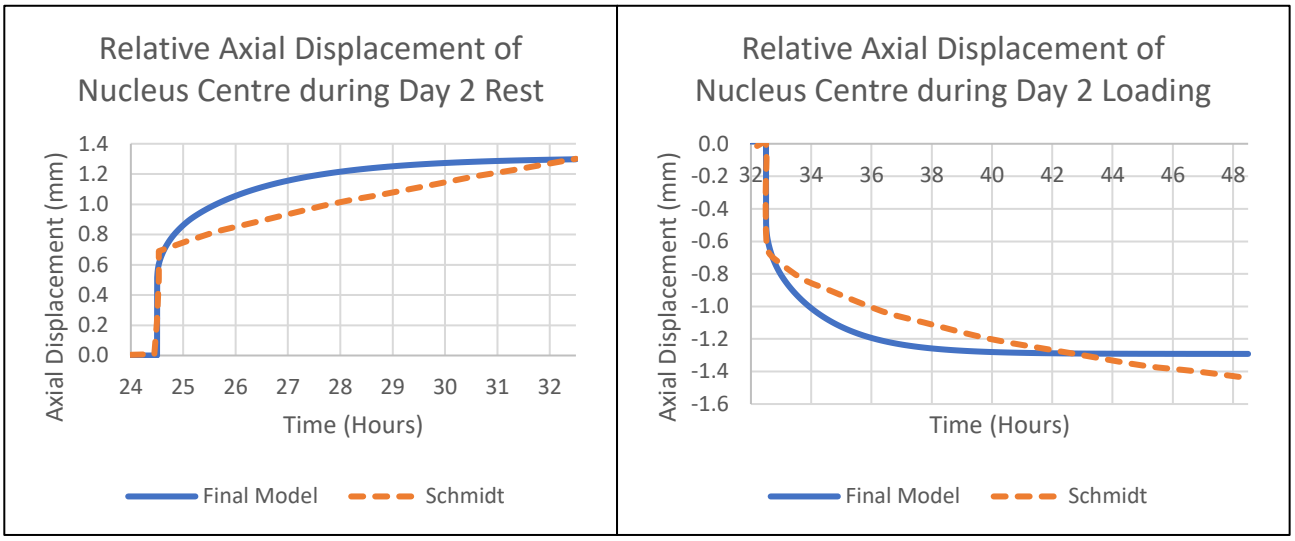

Figure 25: Axial (z) displacement of the centre of the nucleus during the Day 2 Rest period. Note that the displacement has been zeroed at 24 hours, and positive displacement represents movement superiorly. Results approximated from Schmidt et al. (2011).

Figure 26: Axial (z) displacement of the centre of the nucleus during the Day 2 Loading period. Note that the displacement has been zeroed at 32 hours, and positive displacement represents movement superiorly. Results approximated from Schmidt et al. (2011).

As seen in Figure 22, at the end of the Day 1 Loading period the pore pressure was approximately 0MPa throughout the IVD. Immediately after load removal at the start of the Day 2 Rest period, a negative pore pressure was seen with a maximum of -1.28MPa. This negative pore pressure was not constant and varied depending on the position in the IVD. At the end of the Day 2 Rest period, the pore pressure throughout the IVD reached 0MPa. Immediately after load application at the start of the Day 2 Loading period, a positive pore pressure was seen with a maximum of 1.14MPa, which also varied depending on the position in the IVD. The pore pressure throughout the IVD reached 0MPa at the end of the Day 2 Loading period.

The pore pressure contour plots were then compared with those reported by Schmidt et al. (2011). As the load was removed during the start of the Day 2 Rest period, Schmidt's model reported a negative pore pressure with a maximum of -0.4MPa, which was constant throughout the IVD. After the application of load at the start of the Day 2 Loading period, the pore pressure became positive however this varied depending on the region, reaching close to 1.0MPa in the posterior region of the IVD, whereas it reached close to 0.4MPa near the anterior region.

As seen in Figure 22, the pore pressure distribution at the start of the Day 2 Rest period and Day 2 Loading period varied with position. This was highlighted in Figure 23, where the pore pressure was obtained along a path of nodes in the vertical direction. At the start of the Day 2 Rest period, the pore pressure oscillated with vertical position between a negative pore pressure and 0MPa. At the start of the Day 2 Loading period, the pore pressure also oscillated with vertical position between a positive pore pressure and 0MPa.

As seen in Figure 24, immediately following the removal of the load at 24 hours, the pore pressure in the centre of the nucleus for the final model decreased to a peak of -1.23MPa. However, this pore pressure increased over time reaching a steady state of 0MPa after 7.3 hours. As the load was applied at 32 hours, the pore pressure increased to a peak of 1.05MPa, followed by a subsequent decrease to a steady state of 0MPa after 8.9 hours. For Schmidt's model, the pore pressure decreased to -0.4MPa after the removal of the load, and increased to 0.4MPa after the application of the load. The pore pressure in Schmidt's model did not reach steady state during the Day 2 Rest and Day 2 Loading periods.

From Figure 25, as the load was removed during the Day 2 Rest period, the centre of the nucleus moved superiorly. Immediately after load removal, the axial displacement of the final model increased by 0.55mm whereas Schmidt's model increased by 0.65mm. The final model increased exponentially whereas Schmidt's model increased gradually, however both resulted in an axial displacement of 1.3mm at the end of the Day 2 Rest period. As seen in Figure 26, applying the load during the Day 2 Loading period caused the centre of the nucleus to move inferiorly. Immediately after load application, the axial displacement of the final model decreased by 0.55mm whereas Schmidt's model decreased by 0.65mm. At the end of the Day 2 Loading period, the final model decreased to -1.29mm whereas Schmidt's model decreased to -1.45mm.

4.3.3. Discussion

Immediately after the removal of the axial compressive load, a negative pore pressure was seen in the IVD. As the load was removed, this caused the elements in the IVD to undergo volumetric expansion resulting in an increase in pore volume. Negative pore pressures occur when the rate of pore volume increase exceeds the inwards water flow (Li et al., 2023). However, these negative pore pressures in the IVD after unloading have not been reported *in vivo* which means that they are fictive in nature (Schmidt et al., 2011). This negative pore pressure was likely caused by the sudden unloading over 10 seconds, as well as a poorly converged mesh.

Schmidt et al. (2011) found that increasing the duration of unloading as well as further refining a converged mesh, did not eliminate the negative pore pressures. Alternative strategies that were identified in eliminating the negative pore pressures, included decreasing the voids ratio of the nucleus and annulus within the *in vivo* range as well as considering partial saturation of the tissues (Schmidt et al., 2011).

Immediately after the application of load and removal of load, the pore pressure in the IVD oscillated significantly with vertical position. Since the axial compressive load was applied and removed over 10 seconds, this resulted in a loading rate of 0.1Hz. Stokes et al. (2010) found that loading at rapid rates, caused pore pressure oscillations between adjacent elements. These pore pressure oscillations were reduced, by the use of 20-node pore pressure elements (as opposed to 8-node pore pressure elements) as well as the use of biased meshing close to the external boundaries and discontinuities (Stokes et al., 2010).

Since the experimental testing protocols applied loading at various loading rates from 0.001 to 1Hz, these results indicated that the final model would produce pore pressure oscillations at the higher loading rates. To obtain accurate results, it was important to minimise these pore pressure oscillations in the final model by undergoing a mesh convergence study, changing the elements from 8-node pore pressure elements to 20-node pore pressure elements as well as considering biased meshing at the discontinuities (e.g., between the IVD and vertebral bone).

Immediately after the application of load and removal of load, the pore pressure in the centre of the nucleus increased in magnitude to a peak value. However, the peak in the final model was significantly higher than that observed by Schmidt et al. (2011), which indicated that this was likely due to a poorly converged mesh. These results indicated that sudden changes in loading conditions, can cause the pore pressure in the centre of the nucleus to increase in magnitude to a peak value. The pore pressure in the centre of the nucleus, equilibrated with the boundary pore pressure significantly faster in the final model compared to Schmidt et al. (2011). As discussed previously in the verification against Galbusera et al. (2011c), this was likely due to the fact that Schmidt et al. (2011) assigned a boundary pore pressure to all external surfaces of the IVD and vertebral bodies.

The axial displacement of the centre of the nucleus for the final model and Schmidt et al. (2011), was similar at the end of the 8-hours of rest and 16-hours of loading. However, the response differed significantly where the final model increased exponentially whereas Schmidt et al. (2011) increased gradually. Therefore, this verification study verified the pore pressure distribution for the final model, which had several limitations including the presence of negative pore pressures and pore pressure oscillations due to a poorly converged mesh.

5. VALIDATION

5.1. Methodology

The final model was validated against experimental results from the Flinders University Hexapod robot. The experimental data was acquired from the academic supervisor Associate Professor John Costi (Amin, 2019). In the experiment, an L1-L2 FSU was allowed to reach steady-state hydration which represented the lumbar disc during sleeping. An axial compressive preload of 160N was applied for 12 hours, which created an equivalent nucleus pressure of 0.1MPa. The L1 and L2 vertebrae were fixated in cups using PMMA, where the axial compressive preload was applied on the L1 vertebrae whereas the L2 vertebrae was held fixed. This was simulated in the final model, by applying a boundary pore pressure of 0.1MPa on the boundary of the IVD. The axial compressive preload of 160N was applied on the superior surface of the L1 vertebrae, which was applied over 10 seconds and was held for a duration of 12 hours. A fixed support boundary condition was assigned to the inferior surface of the L2 vertebrae.

5.2. Results

The axial displacement of the L1 vertebrae (from the experiment) and the superior surface of the L1 vertebrae (from the final model) were obtained as outputs (Figure 27).

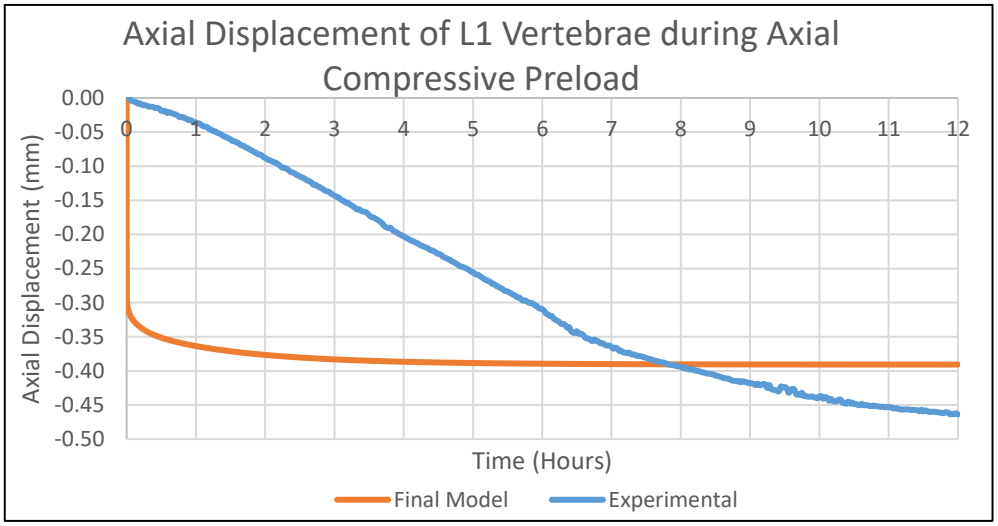

Figure 27: Axial displacement of the L1 vertebrae during the 12-hour axial compressive preload. Note that negative axial displacement represents movement inferiorly. Experimental results provided by Amin (2019).

As seen in Figure 27, the final model and experimental results exhibited significantly different behaviour during the 12-hour axial compressive preload. For the final model, the axial displacement at the start of the simulation instantaneously decreased to -0.14mm followed by an exponential decrease to steady state. For the experimental results, the axial displacement decreased gradually over the 12 hours. The final model reached steady state after 5.3 hours, whereas the experimental

results did not reach steady state. The axial displacement at the end of the 12-hour period, was -0.39mm for the final model and -0.46mm for the experimental results.

5.3. Discussion

The application of the axial compressive preload on the L1 vertebrae, caused the L1 vertebrae to move inferiorly which forced the outflow of fluid in the IVD. However, the response differed significantly between the final model and experimental results. The axial displacement of the L1 vertebrae for the final model decreased in an exponential manner, whereas the experimental results decreased gradually. At the end of the 12-hour axial compressive preload, the axial displacement of the L1 vertebrae showed reasonable agreement between the final model and experimental results.

Since the experimental results were for a single L1-L2 FSU specimen, the physiological response to the axial compressive preload may have varied between different experimental specimens. Although variations between experimental specimens may have played a role in the discrepancies between the final model and experimental results, these were most likely due to the various limitations of the final model. The final model did not fully capture the material behaviour of all tissues in the FSU. The poroelastic properties were only modelled in the nucleus and annulus bulk, whereas they were neglected in the other tissues including the cortical bone, trabecular bone and posterior elements including the facet joints. In the literature, poroelastic properties were typically assigned to the cortical and trabecular bone, however the poroelastic properties in the posterior elements were neglected due to their relatively small thickness (Schmidt et al., 2010).

Since the vertebral bone was not modelled using poroelastic material properties, the fluid flow through the vertebral endplates was also neglected. It has been found that fluid flow through the vertebral endplates is the dominant path of fluid flow compared to the annulus periphery (Schmidt and Shirazi-Adl, 2018). Moreover, the final model assumed a constant tissue permeability for the nucleus and annulus, however the tissue permeability for soft tissues has been shown to decrease exponentially with increasing strains (Schmidt et al., 2011). The final model also neglected the hyperelastic material properties of the IVD (Wagnac et al., 2011), as well as the intrinsic solid-phase viscoelasticity of the IVD due to the sliding and stretching of collagen fibrils (Bezci et al., 2020).

Various tissues were not modelled in the final model including the CEP and BEP, which in the literature were typically assigned using separate material properties. The final model did not model the contact between the facet joints, which significantly limited the physiological relevancy of the model. The facet joints in the lumbar spine are responsible for bearing approximately 6 to 30% of the

axial compressive load depending on the type of loading, and therefore play an important role in load bearing (O'Leary et al., 2018).

Various simplifications were made in the boundary and loading conditions of the final model. In the experiment, the Hexapod robot applied an axial compressive preload of 160N, while the off-axis coupling forces and moments were minimised to zero (Amin, 2019). The final model only applied the axial compressive preload of 160N, however it did not minimise the off-axis coupling forces and moments which may have affected the physiological response.

The axial compressive preload was applied in the axial direction, however this did not account for the curvature of the spine. In the literature, to account for the curvature of the spine, a follower load was applied where the axial compressive preload lied on the tangent of the curve of the lumbar spine (Patwardhan et al., 1999). The follower load technique was found to significantly affect the results, for high axial compressive preloads of greater than 400N (Talukdar et al., 2021). Although the axial compressive preload used in this study (160N) was less than 400N which indicated that the follower load technique would not significantly affect the results, it was important to use the follower load technique for future applications which may require a greater axial compressive preload.

In the experiment, the L1 and L2 vertebrae were fixated in cups using PMMA, where the axial compressive preload was applied on the L1 vertebrae and the L2 vertebrae was held fixed. This was simulated in the final model, by applying the axial compressive preload on the superior surface of the L1 vertebrae, and a fixed support boundary condition on the inferior surface of the L2 vertebrae. Applying the load to the superior surface of the L1 vertebrae, was shown to create significant stress concentrations in the vertebral bone near the applied load. Moreover, evaluating the stresses and strains near the fixed support boundary conditions also produced inaccurate results (Talukdar et al., 2021). However, the results of interest were obtained away from the applied loads and fixed support boundary conditions, which meant that these limitations did not significantly affect the results.

Another significant limitation of this study, was that the mesh used in this project had not undergone a mesh convergence study. As seen in the verification for study 3 (Schmidt et al., 2011), loading at rates of 0.1Hz produced pore pressure oscillations throughout the IVD. Since the experimental testing protocols applied loading at 0.001 to 1Hz, this indicated that further validation at the faster loading rates would produce pore pressure oscillations which would significantly affect the accuracy of the results. To reduce these pore pressure oscillations, it was recommended to use 20-node pore pressure elements and use biased meshing at external boundaries and discontinuities (Schmidt et al., 2011).

6. CONCLUSIONS

No studies in the literature have performed direct validation, of a FE model of the lumbar FSU in all 11 loading directions. Using the FE model of the L1-L2 FSU, this study implemented poroelastic behaviour in the IVD, verified the final model against three studies from the literature which focused on different aspects of the model including the osmotic behaviour, loading behaviour and pore pressure distribution, and conducted direct validation in axial compression. It should be noted that due to the time constraints of the project as well as the steep learning curve for the author, the final model was not able to be directly validated in 11 loading directions.

During the swelling period, the pore pressure in the centre of the nucleus equilibrated with the boundary pore pressure prescribed on the boundary of the IVD. However, the time taken for equilibration was significantly faster in the final model compared to the results from the literature. It was also seen that sudden changes in the displacement and loading conditions, caused a peak in the pore pressure in the centre of the nucleus. For the loading behaviour, the total IVD height lost during the axial compressive loading was less than that reported in the literature. During the axial compressive loading, the final model reached steady state significantly faster than the results from the literature. During periods of unloading, a negative pore pressure was seen throughout the IVD which was not present *in vivo*. Moreover, loading rates of 0.1Hz produced significant pore pressure oscillations throughout the IVD. These pore pressure oscillations showed that direct validation of the model against experimental results at loading rates of 0.1Hz, would produce inaccurate results. The final model was then directly validated against the experimental results during the 12-hour axial compressive preload. The axial displacement of the L1 vertebrae had a significantly different initial response, however the results were in reasonable agreement at the end of the preload.

Although the findings do not support the proposed hypothesis that the final model with poroelastic properties will have close alignment with literature and experimental results, the discrepancies in the results are due to the various limitations of the final model. These limitations include not modelling the vertebral bone using poroelastic behaviour, neglecting fluid flow through the vertebral endplates, assuming a constant permeability, neglecting the hyperelastic and viscoelastic material properties of the IVD, having a poorly converged mesh, not modelling the contact at the facet joints and not applying the axial compressive load as a follower load. This master's research project has laid the foundations for the direct validation of the FE model for the L1-L2 FSU in 11 loading directions. A fully validated FE model of the L1-L2 FSU has various future applications, including the simulation of IVD degeneration and use in the design and development of spinal implants.

7. FUTURE WORK

Since the final model of the L1-L2 FSU had various limitations, the project has significant scope for future work. Initially, the vertebral bone will be modelled using poroelastic behaviour which requires the use of pore pressure elements. The cortical bone will be changed from 4-node shell elements to regular 8-node hexahedral elements. The cortical and trabecular bone will then be changed from 8-node regular elements to 8-node pore pressure elements. Modelling the vertebral bone using poroelastic behaviour will allow fluid flow through the vertebral endplates, which has been shown to be the dominant pathway of fluid flow compared to the annulus periphery. Since the permeability of soft tissues decreases exponentially with increasing strains, the strain-dependent permeability will be implemented on the IVD. The nucleus and annulus will then be updated, to include hyperelastic and viscoelastic material properties.

A mesh convergence study will be undertaken, to ensure that the FE results are independent of the mesh. As per the literature review, mesh convergence is highly direction dependent with axial rotation being the most sensitive loading direction to changes in mesh density. Therefore, a mesh convergence study will be undertaken in axial rotation. The elements used for all poroelastic tissues will be changed from 8-node to 20-node pore pressure elements, to minimise pore pressure oscillations. Since the contact between the facet joints was disabled in the final model due to various convergence issues, the facet joints will be updated to ensure that convergence issues are not encountered. After the completion of each of the preceding tasks, the results will be compared against the three verification studies used during this project, where it is expected that each improvement to the model will improve the correlation with the results from the literature.

To apply loading in the 11 loading directions, a displacement will be applied to the superior surface of the L1 vertebrae at the different loading rates (0.001 to 1Hz) as per the experimental testing sequence. The reaction force on the inferior surface of the L2 vertebrae will be obtained as an output. The force-displacement data will then be obtained for the final model, and the mean squared error will be calculated between the final model and experimental results. The material properties will be optimised to reduce the mean squared error. Therefore, this master's research project has laid the foundations for the direct validation of the FE model for the L1-L2 FSU in 11 loading directions.

8. BIBLIOGRAPHY

Adams, M.A., Dolan, P., 2005. Spine biomechanics. Journal of Biomechanics 38, 1972–1983. https://doi.org/10.1016/j.jbiomech.2005.03.028

Al Qaraghli, M.I., De Jesus, O., 2023. Lumbar Disc Herniation, in: StatPearls. StatPearls Publishing, Treasure Island (FL).

Amin, D., 2019. Analysis of Internal Strains and Mechanics during Simulated Repetitive Lifting Motions in Human Lumber Spinal Segments [WWW Document]. URL https://theses.flinders.edu.au/view/138fe6b6-9628-44be-a49e-82abc4784943/1 (accessed 3.17.23).

Argoubi, M., Shirazi-Adl, A., 1996. Poroelastic creep response analysis of a lumbar motion segment in compression. Journal of Biomechanics 29, 1331–1339. https://doi.org/10.1016/0021-9290(96)00035-8

Asaad, M., Abdul-Sahib, N., Rasheed, M., 2020. Stress and strain analysis of a new design of cervical intervertebral disc under daily activity. IOP Conf. Ser.: Mater. Sci. Eng. 671, 012065. https://doi.org/10.1088/1757-899X/671/1/012065

Australian Commission on Safety and Quality in Healthcare, 2022. A novel approach to break the cycle of low back pain [WWW Document]. A novel approach to break the cycle of low back pain. URL https://www.safetyandquality.gov.au/about-us/latest-news/media-releases/novel-approach-break-cycle-low-back-pain#_edn3

Ayturk, U.M., Puttlitz, C.M., 2011. Parametric convergence sensitivity and validation of a finite element model of the human lumbar spine. Computer Methods in Biomechanics and Biomedical Engineering 14, 695–705. https://doi.org/10.1080/10255842.2010.493517

Bezci, S.E., Lim, S., O'Connell, G.D., 2020. Nonlinear stress-dependent recovery behavior of the intervertebral disc. Journal of the Mechanical Behavior of Biomedical Materials 110, 103881. https://doi.org/10.1016/j.jmbbm.2020.103881

Campbell, J.Q., Coombs, D.J., Rao, M., Rullkoetter, P.J., Petrella, A.J., 2016. Automated finite element meshing of the lumbar spine: Verification and validation with 18 specimen-specific models. Journal of Biomechanics 49, 2669–2676. https://doi.org/10.1016/j.jbiomech.2016.05.025

Chang, T.-S., Chang, J.-H., Cheng, C.-W., 2011. A Pure Moment Based Tester for Spinal Biomechanics, in: Klika, V. (Ed.), Biomechanics in Applications. InTech. https://doi.org/10.5772/21864

Cheung, J.T.-M., Zhang, M., Chow, D.H.-K., 2003. Biomechanical responses of the intervertebral joints to static and vibrational loading: a finite element study. Clinical Biomechanics 18, 790–799. https://doi.org/10.1016/S0268-0033(03)00142-6

Cohen, S.P., Raja, S.N., 2007. Pathogenesis, Diagnosis, and Treatment of Lumbar Zygapophysial (Facet) Joint Pain. Anesthesiology 106, 591–614. https://doi.org/10.1097/00000542-200703000-00024

Dassault Systèmes., 2022a. Pore Fluid Pressure - SIMULIA User Assistance 2022 [WWW Document]. URL https://help.3ds.com/2022/english/dssimulia_established/SIMACAEMATRefMap/simamat-c-porefluidpressure.htm?contextscope=all&id=85c2ce53deb846098410be27494d1db9 (accessed 5.2.23).

Dassault Systèmes., 2022b. Continuity statement for the wetting liquid phase in a porous medium - SIMULIA User Assistance 2022 [WWW Document]. URL https://help.3ds.com/2022/english/dssimulia_established/simacaetherefmap/simathe-c-porcontstate.htm?contextscope=all&highlight=darcy+law&id=3d3a6e715329406f840fc9c4ec5e4080&analyticsContext=search-result&analyticsSearch=darcy%20law&myapp=false (accessed 5.18.23).

Dassault Systèmes., 2022c. Three-Dimensional Solid Element Library - SIMULIA User Assistance 2022 [WWW Document]. URL https://help.3ds.com/2022/english/dssimulia_established/SIMACAEELMRefMap/simaelm-r-3delem.htm?contextscope=all (accessed 5.20.23).

Dassault Systèmes., 2022d. Element formulation and integration - SIMULIA User Assistance 2022 [WWW Document]. URL https://help.3ds.com/2022/english/dssimulia_established/SIMACAEGSARefMap/simagsa-m-CtmElmformint-sb.htm?contextscope=all&id=61daf12ec3184b2090de6647566e4486 (accessed 5.20.23).

Dassault Systèmes., 2022e. Choosing the Appropriate Element for an Analysis Type - SIMULIA User Assistance 2022 [WWW Document]. URL https://help.3ds.com/2022/english/dssimulia_established/SIMACAEELMRefMap/simaelm-c-analysistype.htm?contextscope=all (accessed 9.19.23).

Dassault Systèmes., 2022f. Linear and nonlinear procedures - SIMULIA User Assistance 2022 [WWW Document]. URL https://help.3ds.com/2022/english/dssimulia_established/simacaecaerefmap/simacae-c-simconcunprocs.htm?contextscope=all&highlight=Linear+and+nonlinear+procedures&id=9fcf363fe812495b81fde46bb34e17d1&analyticsContext=search-result&analyticsSearch=Linear%20and%20nonlinear%20procedures&myapp=false (accessed 9.26.23).

Dassault Systèmes., 2022g. Coupled Pore Fluid Diffusion and Stress Analysis - SIMULIA User Assistance 2022 [WWW Document]. URL https://help.3ds.com/2022/english/dssimulia_established/SIMACAEANLRefMap/simaanl-c-coupdiffstress.htm?contextscope=all (accessed 10.2.23).

Dreischarf, M., Zander, T., Shirazi-Adl, A., Puttlitz, C.M., Adam, C.J., Chen, C.S., Goel, V.K., Kiapour, A., Kim, Y.H., Labus, K.M., Little, J.P., Park, W.M., Wang, Y.H., Wilke, H.J., Rohlmann, A., Schmidt, H., 2014. Comparison of eight published static finite element models of the intact lumbar spine: Predictive power of models improves when combined together. Journal of Biomechanics 47, 1757–1766. https://doi.org/10.1016/j.jbiomech.2014.04.002

Ferguson, S.J., Ito, K., Nolte, L.-P., 2004. Fluid flow and convective transport of solutes within the intervertebral disc. Journal of Biomechanics, Spinal Biomechanics 37, 213–221. https://doi.org/10.1016/S0021-9290(03)00250-1

Galbusera, F., Bashkuev, M., Wilke, H.-J., Shirazi-Adl, A., Schmidt, H., 2014. Comparison of various contact algorithms for poroelastic tissues. Computer Methods in Biomechanics and Biomedical Engineering 17, 1323–1334. https://doi.org/10.1080/10255842.2012.745858

Galbusera, F., Schmidt, H., Neidlinger-Wilke, C., Gottschalk, A., Wilke, H.-J., 2011a. The mechanical response of the lumbar spine to different combinations of disc degenerative changes investigated using randomized poroelastic finite element models. Eur Spine J 20, 563–571. https://doi.org/10.1007/s00586-010-1586-4

Galbusera, F., Schmidt, H., Neidlinger-Wilke, C., Wilke, H.-J., 2011b. The effect of degenerative morphological changes of the intervertebral disc on the lumbar spine biomechanics: a poroelastic finite element investigation. Computer Methods in Biomechanics and Biomedical Engineering 14, 729–739. https://doi.org/10.1080/10255842.2010.493522

Galbusera, F., Schmidt, H., Noailly, J., Malandrino, A., Lacroix, D., Wilke, H.-J., Shirazi-Adl, A., 2011c. Comparison of four methods to simulate swelling in poroelastic finite element models of intervertebral discs. Journal of the Mechanical Behavior of Biomedical Materials 4, 1234–1241. https://doi.org/10.1016/j.jmbbm.2011.04.008

Hassan, C.R., Lee, W., Komatsu, D.E., Qin, Y.-X., 2021. Evaluation of nucleus pulposus fluid velocity and pressure alteration induced by cartilage endplate sclerosis using a poro-elastic finite

element analysis. Biomech Model Mechanobiol 20, 281–291. https://doi.org/10.1007/s10237-020-01383-8
Heuer, F., Schmidt, H., Klezl, Z., Claes, L., Wilke, H.-J., 2007. Stepwise reduction of functional spinal structures increase range of motion and change lordosis angle. Journal of Biomechanics 40, 271–280. https://doi.org/10.1016/j.jbiomech.2006.01.007
Jones, A.C., Wilcox, R.K., 2008. Finite element analysis of the spine: Towards a framework of verification, validation and sensitivity analysis. Medical Engineering & Physics, Special issue to commemorate the 30th anniversary of Medical Engineering & Physics 30, 1287–1304. https://doi.org/10.1016/j.medengphy.2008.09.006
Lei, F., Szeri, A.Z., 2007. Inverse analysis of constitutive models: Biological soft tissues. Journal of Biomechanics 40, 936–940. https://doi.org/10.1016/j.jbiomech.2006.03.014
Li, C., Wang, Z., Liu, Q., 2023. Numerical Simulation of Mudstone Shield Tunnel Excavation with ABAQUS Seepage–Stress Coupling: A Case Study. Sustainability 15, 667. https://doi.org/10.3390/su15010667
Little, J.P., Adam, C., 2012. Towards determining soft tissue properties for modelling spine surgery: current progress and challenges. Med Biol Eng Comput 50, 199–209. https://doi.org/10.1007/s11517-011-0848-6
Malandrino, A., Planell, J.A., Lacroix, D., 2009. Statistical factorial analysis on the poroelastic material properties sensitivity of the lumbar intervertebral disc under compression, flexion and axial rotation. Journal of Biomechanics 42, 2780–2788. https://doi.org/10.1016/j.jbiomech.2009.07.039
Meng, Q., Jin, Z., Fisher, J., Wilcox, R., 2013. Comparison between FEBio and Abaqus for biphasic contact problems. Proc Inst Mech Eng H 227, 1009–1019. https://doi.org/10.1177/0954411913483537
Natarajan, R.N., Williams, J.R., Lavender, S.A., Andersson, G.B.J., 2007. Poro-elastic finite element model to predict the failure progression in a lumbar disc due to cyclic loading. Computers & Structures, Fourth MIT Conference on Computational Fluid and Solid Mechanics 85, 1142–1151. https://doi.org/10.1016/j.compstruc.2006.08.043
Newell, N., Little, J., Christou, A., Adams, M., Adam, C., Masouros, S., 2017. Biomechanics of the human intervertebral disc: A review of testing techniques and results. Journal of the Mechanical Behavior of Biomedical Materials 69, 420–434. https://doi.org/10.1016/j.jmbbm.2017.01.037
Nikkhoo, M., Hsu, Y.-C., Haghpanahi, M., Parnianpour, M., Wang, J.-L., 2013. A meta-model analysis of a finite element simulation for defining poroelastic properties of intervertebral discs. Proc Inst Mech Eng H 227, 672–682. https://doi.org/10.1177/0954411913480668
Oftadeh, R., Connizzo, B.K., Nia, H.T., Ortiz, C., Grodzinsky, A.J., 2018. Biological connective tissues exhibit viscoelastic and poroelastic behavior at different frequency regimes: Application to tendon and skin biophysics. Acta Biomaterialia 70, 249–259. https://doi.org/10.1016/j.actbio.2018.01.041
O'Leary, S.A., Paschos, N.K., Link, J.M., Klineberg, E.O., Hu, J.C., Athanasiou, K.A., 2018. Facet Joints of the Spine: Structure–Function Relationships, Problems and Treatments, and the Potential for Regeneration. Annual Review of Biomedical Engineering 20, 145–170. https://doi.org/10.1146/annurev-bioeng-062117-120924
Patwardhan, A.G., Havey, R.M., Meade, K.P., Lee, B., Dunlap, B., 1999. A Follower Load Increases the Load-Carrying Capacity of the Lumbar Spine in Compression. Spine 24, 1003.
Renner, S.M., Natarajan, R.N., Patwardhan, A.G., Havey, R.M., Voronov, L.I., Guo, B.Y., Andersson, G.B.J., An, H.S., 2007. Novel model to analyze the effect of a large compressive follower pre-load on range of motions in a lumbar spine. Journal of Biomechanics 40, 1326–1332. https://doi.org/10.1016/j.jbiomech.2006.05.019

Schmidt, H., Bashkuev, M., Dreischarf, M., Rohlmann, A., Duda, G., Wilke, H.-J., Shirazi-Adl, A., 2013. Computational biomechanics of a lumbar motion segment in pure and combined shear loads. Journal of Biomechanics 46, 2513–2521. https://doi.org/10.1016/j.jbiomech.2013.06.038

Schmidt, H., Galbusera, F., Wilke, H.-J., Shirazi-Adl, A., 2011. Remedy for fictive negative pressures in biphasic finite element models of the intervertebral disc during unloading. Computer Methods in Biomechanics and Biomedical Engineering 14, 293–303. https://doi.org/10.1080/10255842.2010.481287

Schmidt, H., Heuer, F., Drumm, J., Klezl, Z., Claes, L., Wilke, H.-J., 2007. Application of a calibration method provides more realistic results for a finite element model of a lumbar spinal segment. Clinical Biomechanics 22, 377–384. https://doi.org/10.1016/j.clinbiomech.2006.11.008

Schmidt, H., Shirazi-Adl, A., 2018. Temporal and spatial variations of pressure within intervertebral disc nuclei. Journal of the Mechanical Behavior of Biomedical Materials 79, 309–313. https://doi.org/10.1016/j.jmbbm.2018.01.012

Schmidt, H., Shirazi-Adl, A., Galbusera, F., Wilke, H.-J., 2010. Response analysis of the lumbar spine during regular daily activities—A finite element analysis. Journal of Biomechanics 43, 1849–1856. https://doi.org/10.1016/j.jbiomech.2010.03.035

Silva, P., Crozier, S., Veidt, M., Pearcy, M.J., 2005. An experimental and finite element poroelastic creep response analysis of an intervertebral hydrogel disc model in axial compression. J Mater Sci: Mater Med 16, 663–669. https://doi.org/10.1007/s10856-005-2538-0

Stokes, I.A., Chegini, S., Ferguson, S.J., Gardner-Morse, M.G., Iatridis, J.C., Laible, J.P., 2010. Limitation of Finite Element Analysis of Poroelastic Behavior of Biological Tissues Undergoing Rapid Loading. Ann Biomed Eng 38, 1780–1788. https://doi.org/10.1007/s10439-010-9938-0

Talukdar, R.G., Mukhopadhyay, K.K., Dhara, S., Gupta, S., 2021. Numerical analysis of the mechanical behaviour of intact and implanted lumbar functional spinal units: Effects of loading and boundary conditions. Proc Inst Mech Eng H 235, 792–804. https://doi.org/10.1177/09544119211008343

Velísková, P., Bashkuev, M., Shirazi-Adl, A., Schmidt, H., 2018. Computational study of the role of fluid content and flow on the lumbar disc response in cyclic compression: Replication of in vitro and in vivo conditions. Journal of Biomechanics, 2nd International Workshop on Spine Loading and Deformation 70, 16–25. https://doi.org/10.1016/j.jbiomech.2017.10.032

Wagnac, E., Arnoux, P.-J., Garo, A., El-Rich, M., Aubin, C.-E., 2011. Calibration of Hyperelastic Material Properties of the Human Lumbar Intervertebral Disc under Fast Dynamic Compressive Loads. Journal of Biomechanical Engineering 133. https://doi.org/10.1115/1.4005224

Williamson, O., Cameron, P., 2021. The Global Burden of Low Back Pain. International Association for the Study of Pain (IASP). URL https://www.iasp-pain.org/resources/fact-sheets/the-global-burden-of-low-back-pain/ (accessed 3.30.23).

Xu, M., Yang, J., Lieberman, I.H., Haddas, R., 2017. Lumbar spine finite element model for healthy subjects: development and validation. Computer Methods in Biomechanics and Biomedical Engineering 20, 1–15. https://doi.org/10.1080/10255842.2016.1193596

Zanjani-Pour, S., Winlove, C.P., Smith, C.W., Meakin, J.R., 2016. Image driven subject-specific finite element models of spinal biomechanics. Journal of Biomechanics, SI: Spine Loading and Deformation 49, 919–925. https://doi.org/10.1016/j.jbiomech.2016.02.025

Zheng, L., Cao, Y., Yang, Y., Xu, M., Zeng, H., Zhu, S., Candito, A., Chen, Y., Zhu, R., Cheng, L., 2022. Biomechanical response of lumbar intervertebral disc in daily sitting postures: a poroelastic finite element analysis. Computer Methods in Biomechanics and Biomedical Engineering 0, 1–10. https://doi.org/10.1080/10255842.2022.2159760

Zirbel, S.A., Stolworthy, D.K., Howell, L.L., Bowden, A.E., 2013. Intervertebral disc degeneration alters lumbar spine segmental stiffness in all modes of loading under a compressive follower load. The Spine Journal 13, 1134–1147. https://doi.org/10.1016/j.spinee.2013.02.010

9. APPENDICES

Appendix A: Gantt chart

The timeline for this project can be seen in the Gantt chart in Figure 28.

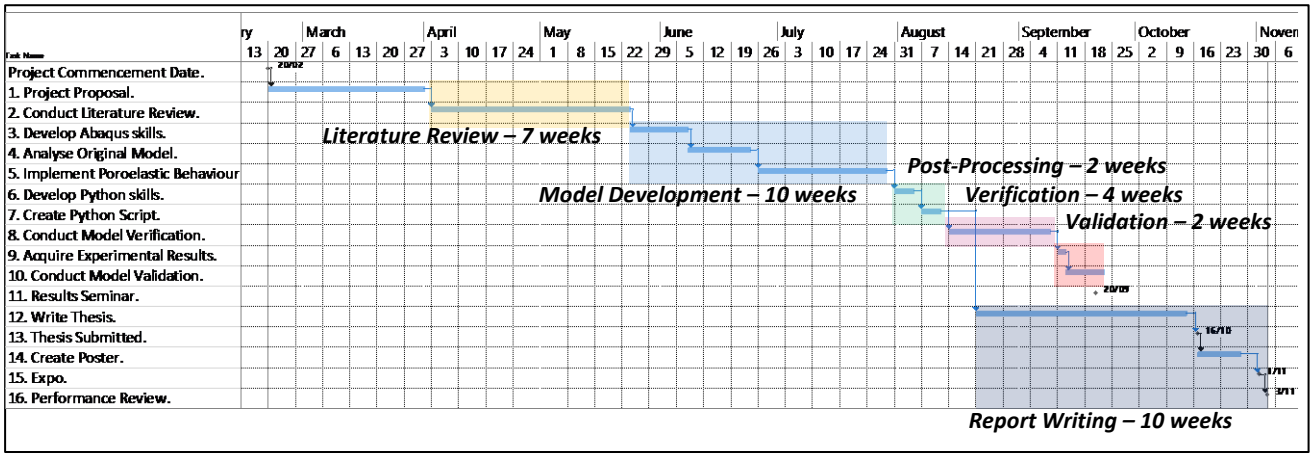

Figure 28: Timeline for the project.

Appendix B: Literature Review

Appendix B1: Material properties

Table 4: The material behaviour used in each study as well as for each individual tissue is shown, where "E" represents elastic material behaviour, "P" represent poroelastic material behaviour and "PH" represents porohyperelastic material behaviour. A dash ("-") indicates that the information is not available, since the information was not reported in the study.

Tissue	Material Properties	Argoubi and Shirazi-Adl (1996)	Malandrino et al. (2009)	Cheung et al. (2003)	Ferguson et al. (2004)	Zheng et al. (2022)	Schmidt et al. (2013)	Galbusera et al. (2011b)
	Lumbar segment	L2-L3 FSU	L3-L4 IVD	L4-L5 FSU	Generic IVD with adjacent bone	L4-L5 FSU	L4-L5 FSU	L4-L5 FSU
Nucleus	Material Behaviour	P	P	P	P	PH	PH	PH
	Elastic Modulus E (MPa)	1.5	1 or 1.66	1	1.5	Neo-Hookean	Neo-Hookean	Neo-Hookean
	Poisson's ratio v	0.1	0.17	0.1	0.17	Neo-Hookean	Neo-Hookean	Neo-Hookean
	Initial permeability k_o (m^4/Ns)	3.00E-16	7.50E-16 or 1.40E-15	3.00E-16	7.50E-16	3.00E-16	2.13E-15	7.50E-16
	Initial voids ratio e_o	4	-	4	4	4	4.88	4
	M Value	10	-	10	8.5	10	10	8.5
	Initial Porosity n_o	-	0.71	-	-	-	-	-
Annulus Bulk	Material Behaviour	P	P	P	P	PH	PH	PH
	Elastic Modulus E (MPa)	2.5	2.56 or 12.29	4.2	2.5	Neo-Hookean	Neo-Hookean	Neo-Hookean
	Poisson's ratio v	0.1	0.35	0.1	0.17	Neo-Hookean	Neo-Hookean	Neo-Hookean
	Initial permeability k_o (m^4/Ns)	3.00E-16	7.50E-16 or 1.87E-15	3.00E-16	7.50E-16	3.00E-16	Anisotropic.	7.50E-16
	Initial voids ratio e_o	2.33	-	2.33	4	2.33	2.33	2.33
	M Value	12	-	12	8.5	12	12	8.5
	Initial Porosity n_o	-	0.57	-	-	-	-	-
Annulus Fibres	Material Behaviour	-	-	E	E	-	-	-
	Elastic Modulus E (MPa)	-	-	500	60	-	-	-
	Poisson's ratio v	-	-	0.3	0.33	-	-	-
CEP	Material Behaviour	P	P	P	-	P	P	P
	Elastic Modulus E (MPa)	5	5	25	-	23.8	5	5
	Poisson's ratio v	0.1	0.17	0.1	-	0.4	0.17	0.1
	Initial permeability k_o (m^4/Ns)	7.00E-15	1.00E-16 or 1.40E-15	7.00E-15	-	7.00E-15	7.00E-15	7.50E-15
	Initial voids ratio e_o	4	-	4	-	4	5	4
	M Value	10	-	10	-	10	10	8.5
	Initial Porosity n_o	-	0.8	-	-	-	-	-
BEP	Material Behaviour	-	P	-	P	-	P	-
	Elastic Modulus E (MPa)	-	1000	-	10000	-	10000	-
	Poisson's ratio v	-	0.3	-	0.3	-	0.3	-
	Initial permeability k_o (m^4/Ns)	-	2.00E-07	-	2.00E-07	-	1.00E-21	-
	Initial voids ratio e_o	-	-	-	0.05	-	0.05	-

Tissue	Material Properties	Argoubi and Shirazi-Adl (1996)	Malandrino et al. (2009)	Cheung et al. (2003)	Ferguson et al. (2004)	Zheng et al. (2022)	Schmidt et al. (2013)	Galbusera et al. (2011b)
	M Value	-	-	-	-	-	12	-
	Initial Porosity n_o	-	0.048	-	-	-	-	-
Cortical Bone	**Material Behaviour**	P	P	E	P	P	P	P
	Elastic Modulus E (MPa)	10000	Anisotropic: 8000, 8000, 12000	12000	10000	10000	10000	10000
	Poisson's ratio v	0.3	Anisotropic: 0.4, 0.23, 0.35	0.3	0.3	0.3	0.3	0.3
	Initial permeability k_o (m^4/Ns)	1.00E-20	5.00E-12	-	5.00E-12	1.00E-20	5.00E-12	5.00E-12
	Initial voids ratio e_o	0.02	-	-	0.05	0.02	0.02	0.05
	M Value	22	-	-	-	22	22	-
	Initial Porosity n_o	-	0.048	-	-	-	-	-
Trabecular Bone	**Material Behaviour**	P	P	P	P	P	P	P
	Elastic Modulus E (MPa)	100	Anisotropic: 140, 140, 250	100	100	100	100	100
	Poisson's ratio v	0.2	Anisotropic: 0.45, 0.176, 0.315	0.2	0.2	0.2	0.2	0.2
	Initial permeability k_o (m^4/Ns)	1.00E-16	2.68E-8 or 2.00E-7	1.00E-13	2.00E-07	1.00E-13	1.00E-07	2.00E-07
	Initial voids ratio e_o	0.4	-	0.4	1	0.4	1	1
	M Value	18	-	18	-	18	-	-

Appendix B2: Supplementary Section for Chapter 2.3. Calibration

An algorithm to optimise the poroelastic material properties for articular cartilage was developed by Lei and Szeri (2007), which used MATLAB (2022b, The MathWorks, Natick, MA, USA) to interface with Abaqus and FORTRAN (2018, IBM, Armonk, NY, USA). The ‘‘lsqnonlin” MATLAB function was used to conduct a nonlinear least-squares optimisation between the theoretical and experimental force-displacement data, where the error between the theoretical and experimental force values was calculated and minimised. Two material properties were independently adjusted while keeping all other properties constant, which showed effective convergence after minimal number of iterations. For optimising six material properties, this algorithm required a significant number of iterations (54) to achieve convergence, however this was reduced if the properties were assigned close to the target values (Lei and Szeri, 2007).

Nikkhoo et al. (2013) also developed an algorithm to optimise the poroelastic material properties of porcine IVD. Three material properties including the elastic modulus, permeability and poisson’s ratio of the annulus were independently varied, and a ratio was used to calculate the material properties of the nucleus. The cumulative deviation between the theoretical and experimental deformations was then calculated, and this was iteratively reduced to less than 5%. When optimising for three material properties in the same porcine IVD model, the algorithm developed by Nikkhoo et al. (2013) required 13 simulations to achieve convergence, whereas the algorithm developed by Lei and Szeri (2007) required 80-150 simulations to achieve the same convergence (Nikkhoo et al., 2013).

In contrast, Schmidt et al. (2007) performed calibration on the L4-L5 FSU by reducing the number of tissues and adding tissues in a stepwise manner, where each configuration was calibrated against experimental data for the reduced specimens. Initially, the FE model consisted of the annulus and this was calibrated against experimental data. The other structures including the nucleus, six major ligaments and posterior elements were then added in a stepwise manner and during each step, the model was calibrated against the experimental data for the reduced specimens (Schmidt et al., 2007).

Appendix C: MATLAB Script for creating Node and Element Sets

```
% Note that the folder of the MATLAB code should have:
%   - MATLAB Code
%   - Text files with name: "node_IVD"
%                           "node_IVD_SuperiorSurface"
%                           "node_IVD_InferiorSurface"
%                           "elem_Annulus"
%                           "elem_Nucleus_FluidCavity"
%   - Folders with name:    "Export - Annulus and Nucleus Node Matrix"
%                           "Export - IVD Boundary Node"
%                           "Export - Nucleus Boundary Node"
%                           "Export - Nucleus Element Matrix"

close all; clear all;

%% Options
% Turn on or off depending on which plot is desired
plot_IVD_Node='off';
plot_NucleusAndAnnulus_Node='off';
plotNodeCrossSection='off';
plotMeshCrossSection='off';
plotL1L2Nucleus='off';
plotMesh='off';
% Turn on or off depending on which variable is to be exported
exportNucleusElement='off';
exportAnnNucNodes='off';
exportIVDBoundaryNode='off';
exportNucleusBoundary='off';

%% Read the text files located in the same folder

% This should have the format:
% Nodes: Node ID, x-coordinate, y-coordinate, z-coordinate
% Node sets: Up to 16 node IDs in each row
% Elements: Element ID, node ID for each element

%Node matrix for all nodes in IVD
node_IVD = readmatrix("node_IVD");

%Node matrix for nodes on IVD Superior Surface
node_IVD_Superior = readmatrix("node_IVD_SuperiorSurface");

%Node matrix for nodes on IVD Inferior Surface
node_IVD_Inferior = readmatrix("node_IVD_InferiorSurface");

%Element connectivity matrix for Annulus
elem_Annulus = readmatrix("elem_Annulus");

%Element connectivity matrix for Nucleus Fluid Cavity
elem_Nucleus_FluidCavity = readmatrix("elem_Nucleus_FluidCavity");

%% Find node matrix for Annulus

% Find all unique nodes in Annulus region
% Obtain node ID for all elements
node_Annulus_All = elem_Annulus(:,2:9);
% Reshape matrix into a column matrix
node_Annulus_All_Resized = reshape(node_Annulus_All,8*length(node_Annulus_All),1);
% Find all unique nodes in the annulus region
node_Annulus = unique(node_Annulus_All_Resized);
```

```
% Find x,y,z coordinates for all nodes in the annulus node matrix
% For each node ID in the annulus node matrix, use the find() function to find
% this node ID in the IVD node matrix, and copy the x,y,z coordinates appropriately
index1=1;
for i=1:length(node_Annulus)
    index2=find(node_Annulus(i,1)==node_IVD(:,1));
    node_Annulus(index1,2:4)=node_IVD(index2,2:4);
    index1=index1+1;
end

%% Find node matrix for Nucleus

% Find all unique nodes on Nucleus Fluid Cavity
% Obtain node ID for all elements
node_Nucleus_FluidCavityAll = elem_Nucleus_FluidCavity(:,2:5);
% Reshape matrix into a column matrix
node_Nucleus_FluidCavityAll_Resized =
reshape(node_Nucleus_FluidCavityAll,4*length(node_Nucleus_FluidCavityAll),1);
% Find all unique nodes
node_Nucleus_FluidCavity = unique(node_Nucleus_FluidCavityAll_Resized);
% Find nodes on the Nucleus-Annulus boundary
node_Nucleus_Annulus_Boundary = node_Nucleus_FluidCavity(101:320);

% Find x,y,z coordinates for all nodes in the node_Nucleus_FluidCavity matrix
index3=1;
for i=1:length(node_Nucleus_FluidCavity)
    index4=find(node_Nucleus_FluidCavity(i,1)==node_IVD(:,1));
    node_Nucleus_FluidCavity(index3,2:4)=node_IVD(index4,2:4);
    index3=index3+1;
end

% Find nodes located in Annulus region not including nodes on the Nucleus Fluid Cavity
node_Annulus_Exclusive = node_Annulus;
for i=1:length(node_Nucleus_FluidCavity)
    if all(ismember(node_Nucleus_FluidCavity(i,1),node_Annulus_Exclusive(:,1)))
        index5=find(node_Nucleus_FluidCavity(i,1)==node_Annulus_Exclusive(:,1));
        node_Annulus_Exclusive(index5,:)=[];
    end
end

% Initialise Nucleus nodes matrix
node_Nucleus = zeros();

% Find if the nodes are located in the Annulus region
% If the nodes are located outside the Annulus region or on the boundary of Nucleus-
Annulus,
% then assign them to the Nucleus region
index6=1;
for i=1:length(node_IVD)
    if ismember(node_IVD(i,1),node_Annulus_Exclusive(:,1))
    else
        node_Nucleus(index6,1:4)=node_IVD(i,1:4);
        index6=index6+1;
    end
end

%% Define element connectivity matrix for Nucleus

% Plot Nucleus nodes (side and cross-section view of ground layer)
if strcmp(plotNodeCrossSection,'on')==1
    % Plot side view
    figure; hold all; axis equal; xlabel('y-axis'); ylabel('z-axis');
    xlim([-80 -40]);
```

```
    ylim([-45 -25]);
    index7=1;
    for i=1:7
        plot(node_Nucleus(index7:index7+99,3),node_Nucleus(index7:index7+99,4),'-o');
        index7=index7+100;
    end

    % Plot cross-section view of ground layer
    figure; hold all; axis equal; xlabel('y-axis'); ylabel('x-axis');
    P1=plot(node_Nucleus(1:44,3),node_Nucleus(1:44,2),'-o'); % Outer ring section
    P2=plot(node_Nucleus(45:70,3),node_Nucleus(45:70,2),'-o'); % Inner ring section
    P3=plot(node_Nucleus(71:100,3),node_Nucleus(71:100,2),'-o'); % Zig-zag section

    % Add element IDs to each node in the cross-section view plot
    % This is displayed alongside the XY-coordinates of each node
    nodeID=cell(1,length(node_Nucleus(1:100,:)));
    for i=1:length(node_Nucleus(1:100,:))
        nodeID{i}=num2str(node_Nucleus(i,1));
    end
    tipData1=dataTipTextRow('ID =',nodeID(1:44));
    tipData2=dataTipTextRow('ID =',nodeID(45:70));
    tipData3=dataTipTextRow('ID =',nodeID(71:100));
    P1.DataTipTemplate.DataTipRows(end+1)=tipData1;
    P2.DataTipTemplate.DataTipRows(end+1)=tipData2;
    P3.DataTipTemplate.DataTipRows(end+1)=tipData3;
end

NoE=0; %Number of elements.
% Initialise Nucleus elements matrix
elem_Nucleus=zeros(0,9);

OR=node_Nucleus(1:44,1); %outer ring section
IR=node_Nucleus(45:70,1); %inner ring section
ZZ=node_Nucleus(71:100,1); %zig-zag section
i1=1;
j1=1;
%Elements between outer ring and inner ring section
for i=1:35
    if i==4 || i==6 || i==10 || i==14 || i==18 || i==22 || i==27 || i==29 || i==33
        elem_Nucleus(i,2:5)=[OR(i1,1),OR(i1+1,1),OR(i1+2,1),IR(j1,1)];
        i1=i1+2;
        j1=j1;
    elseif i==35
        elem_Nucleus(i,2:5)=[OR(i1,1),OR(1,1),IR(1,1),IR(j1,1)];
    else
        elem_Nucleus(i,2:5)=[OR(i1,1),OR(i1+1,1),IR(j1+1,1),IR(j1,1)];
        i1=i1+1;
        j1=j1+1;
    end
    NoE=NoE+1;
end

% Elements between inner ring and zig-zag section
j1=1;
k1=16;
for i=1:22
   if i>=1 && i<=3
        elem_Nucleus(i+35,2:5)=[IR(j1,1),IR(j1+1,1),ZZ(k1-5,1),ZZ(k1,1)];
        j1=j1+1;
        k1=k1-5;
   elseif i==4 || i==9 || i==15 || i==20
       elem_Nucleus(i+35,2:5)=[IR(j1,1),IR(j1+1,1),IR(j1+2,1),ZZ(k1,1)];
       j1=j1+2;
```

```
    elseif i>=5 && i<=8
        elem_Nucleus(i+35,2:5)=[IR(j1,1),IR(j1+1,1),ZZ(k1+1,1),ZZ(k1,1)];
        j1=j1+1;
        k1=k1+1;
    elseif i>=10 && i<=14
        elem_Nucleus(i+35,2:5)=[IR(j1,1),IR(j1+1,1),ZZ(k1+5,1),ZZ(k1,1)];
        j1=j1+1;
        k1=k1+5;
    elseif i>=16 && i<=19
        elem_Nucleus(i+35,2:5)=[IR(j1,1),IR(j1+1,1),ZZ(k1-1,1),ZZ(k1,1)];
        j1=j1+1;
        k1=k1-1;
    elseif i==21
         elem_Nucleus(i+35,2:5)=[IR(j1,1),IR(j1+1,1),ZZ(k1-5,1),ZZ(k1,1)];
         j1=j1+1;
         k1=k1-5;
    elseif i==22
        elem_Nucleus(i+35,2:5)=[IR(j1,1),IR(1,1),ZZ(k1-5,1),ZZ(k1,1)];
    end
    NoE=NoE+1;
end

% Elements in zig-zag Section
k1=1;
for i=1:20
    elem_Nucleus(i+35+22,2:5)=[ZZ(k1,1),ZZ(k1+1,1),ZZ(k1+6,1),ZZ(k1+5,1)];
    if mod(i,4)==0
        k1=k1+2;
    else
        k1=k1+1;
    end
    NoE=NoE+1;
end

% Create the nucleus element connectivity matrix by connecting each node to
% the corresponding nodes on the layers above and below
elem_Nucleus(1:NoE,6:9)=elem_Nucleus(1:NoE,2:5)+1000;
for i=1:5 %% number of layers in z-direction (6 layers in this case)
    elem_Nucleus((i*NoE)+1:(i+1)*NoE,2:9)=elem_Nucleus(1:NoE,2:9)+1000*i;
end

% Define element IDs for the nucleus elements.
ID=2665601;
for i=1:length(elem_Nucleus)
    elem_Nucleus(i,1)=ID;
    ID=ID+1;
end

%% Node Set - IVD Boundary
%Reshape nodes matrix for IVD Superior Surface and IVD Inferior Surface
nodeIVDInferior = reshape(node_IVD_Inferior',[],1);
nodeIVDInferior(any(isnan(nodeIVDInferior),2),:)=[];

nodeIVDSuperior = reshape(node_IVD_Superior',[],1);
nodeIVDSuperior(any(isnan(nodeIVDSuperior),2),:)=[];

nodeIVDOuter=[];
nodeIVDOuter(:,1)=nodeIVDInferior(:,1);
L1=1000;
for i=1:5
    nodeIVDOuter(end+1:end+44,1)=node_Annulus(1:44)+L1;
    L1=L1+1000;
end
```

```
nodeIVDOuter(end+1:end+length(nodeIVDSuperior),1)=nodeIVDSuperior(:,1);

%Add x,y,z coordinates
I7=1;
for i=1:length(nodeIVDOuter(:,1))
    I8=find(nodeIVDOuter(i,1)==node_IVD(:,1));
    nodeIVDOuter(I7,2:4)=node_IVD(I8,2:4);
    I7=I7+1;
end

%% Plot L1L2 Nodes
if strcmp(plotL1L2Nucleus,'on')==1
    figure;
    hold all;axis equal;xlabel('x-axis');ylabel('y-axis');zlabel('z-axis');
    plot3(node_IVD(:,2),node_IVD(:,3),node_IVD(:,4),'.','Color','r','MarkerSize',10);
%
plot3(node_Nucleus_FluidCavity(:,2),node_Nucleus_FluidCavity(:,3),node_Nucleus_FluidCavity
(:,4),'-','Color','b','LineWidth',3);
    plot3(node_Nucleus(:,2),node_Nucleus(:,3),node_Nucleus(:,4),'-
','Color','b','LineWidth',3);
end

%% Plot Nodes
if strcmp(plot_IVD_Node,'on')==1 | strcmp(plot_NucleusAndAnnulus_Node,'on')==1
    figure;
    hold all;axis equal;xlabel('x-axis');ylabel('y-axis');zlabel('z-axis');
    ylim([-90 -30]);
    xlim([50 95]);
    view(-90,90);

    if strcmp(plot_IVD_Node,'on')==1
      plot3(node_IVD(:,2),node_IVD(:,3),node_IVD(:,4),'ok','MarkerSize',6);
      h = legend('IVD Node Set');
    elseif strcmp(plot_NucleusAndAnnulus_Node,'on')==1

plot3(node_Annulus(:,2),node_Annulus(:,3),node_Annulus(:,4),'o','MarkerFaceColor',[0.588
0.761 0.788],'MarkerSize',6);

plot3(node_Nucleus(:,2),node_Nucleus(:,3),node_Nucleus(:,4),'o','MarkerFaceColor',[0.788
0.616 0.588],'MarkerSize',6);
      h = legend('Annulus Node Set','Nucleus Node Set');
    end



    set(gcf,'Position',get(0,'screensize'))
    set(h,'FontSize',16);
    set(h,'Location','north');
end

if strcmp(plotMeshCrossSection,'on')==1
    figure; hold all; axis equal; xlabel('x-axis'); ylabel('y-axis');
    for i=1:NoE
        p1=knnsearch(node_IVD(:,1),elem_Nucleus(i,2));
        p2=knnsearch(node_IVD(:,1),elem_Nucleus(i,3));
        p3=knnsearch(node_IVD(:,1),elem_Nucleus(i,4));
        p4=knnsearch(node_IVD(:,1),elem_Nucleus(i,5));

        patch([node_IVD(p1,2) node_IVD(p2,2) node_IVD(p3,2) node_IVD(p4,2)], ...
            [node_IVD(p1,3) node_IVD(p2,3) node_IVD(p3,3) node_IVD(p4,3)],'white');
    end
end
```

```
%% Plot Elements
if strcmp(plotMesh,'on')==1
    figure; hold all; xlabel('x-axis (mm)'); ylabel('y-axis (mm)'); zlabel('z-axis (mm)')
    set(gcf,'Position',get(0,'screensize'))
%     ylim([-90 -30]);
%     xlim([50 95]);
    view(-45,45);
    for i=1:length(elem_Nucleus) % for all elements
    index4=knnsearch(node_IVD(:,1),transpose(elem_Nucleus(i,2:9)));
    coord=node_IVD(index4,2:4);
    index6=1;
    for k=1:3

xyzCoord(:,index6:index6+5)=[coord(1,k),coord(1,k),coord(2,k),coord(3,k),coord(1,k),coord(
5,k);

coord(2,k),coord(2,k),coord(3,k),coord(4,k),coord(4,k),coord(6,k);

coord(6,k),coord(3,k),coord(7,k),coord(8,k),coord(8,k),coord(7,k);

coord(5,k),coord(4,k),coord(6,k),coord(7,k),coord(5,k),coord(8,k)];
        index6=index6+6;
    end
    fill3(xyzCoord(:,1:6),xyzCoord(:,7:12),xyzCoord(:,13:18),[0.788 0.616 0.588]);
    end

end

%% Export node sets and element sets

exportNodeAnnulus=zeros();
exportNodeNucleus=zeros();
exportIVDBoundary=zeros();
exportNodeNucleusBoundary=zeros();
r=1;
P3=1;
for i=1:length(node_Annulus_Exclusive(:,1))
    exportNodeAnnulus(r,P3)=node_Annulus_Exclusive(i,1);
    P3=P3+1;
    if mod(i,16)==0
        r=r+1;
        P3=1;
    end
end
r=1;
P3=1;
for i=1:length(node_Nucleus(:,1))
    exportNodeNucleus(r,P3)=node_Nucleus(i,1);
    P3=P3+1;
    if mod(i,16)==0
        r=r+1;
        P3=1;
    end
end
r=1;
P3=1;
for i=1:length(nodeIVDOuter(:,1))
    exportIVDBoundary(r,P3)=nodeIVDOuter(i,1);
    P3=P3+1;
    if mod(i,16)==0
        r=r+1;
        P3=1;
    end
```

```
end
r=1;
P3=1;
for i=1:length(node_Nucleus_FluidCavity(:,1))
    exportNodeNucleusBoundary(r,P3)=node_Nucleus_FluidCavity(i,1);
    P3=P3+1;
    if mod(i,16)==0
        r=r+1;
        P3=1;
    end
end
% Export nucleus element set
if strcmp(exportNucleusElement,'on')==1
    path='C:\Users\nishu\OneDrive - Flinders\Documents 1\,Laptop\Project\5.
Methods\MATLAB\Create Node-Element Sets\Export - Nucleus Element Matrix\';
    fileName=[path,'L1L2NucleusElem',datestr(now,' mm-dd-yyyy HH-MM-SS'),'.txt'];
    writematrix(elem_Nucleus,fileName,'Delimiter',',');
end
% Export node set for just the nucleus and just the annulus
if strcmp(exportAnnNucNodes,'on')==1
    path='C:\Users\nishu\OneDrive - Flinders\Documents 1\,Laptop\Project\5.
Methods\MATLAB\Create Node-Element Sets\Export - Annulus and Nucleus Node Matrix\';

    fileName1=[path,'L1L2NodeSet',datestr(now,' mm-dd-yyyy HH-MM-SS'),' Annulus ','.txt'];
    writematrix(exportNodeAnnulus,fileName1,'Delimiter',',');
    data1=readlines(fileName1);
    ix1=strlength(data1)>0;
    data1(ix1)=strcat(data1(ix1),",");
    writematrix(data1,fileName1,'QuoteStrings','none');

    fileName2=[path,'L1L2NodeSet',datestr(now,' mm-dd-yyyy HH-MM-SS'),' Nucleus','.txt'];
    writematrix(exportNodeNucleus,fileName2,'Delimiter',',');
    data2=readlines(fileName2);
    ix2=strlength(data2)>0;
    data2(ix2)=strcat(data2(ix2),",");
    writematrix(data2,fileName2,'QuoteStrings','none');
    %Make sure to remove 0 at the end of the text file
end
% Export node set for boundary of IVD
if strcmp(exportIVDBoundaryNode,'on')==1
    path='C:\Users\bazz0003\OneDrive - Flinders\Documents 1\,Laptop\Project\5.
Methods\MATLAB\Create Node-Element Sets\Export - IVD Boundary Node\';

    fileName3=[path,'IVDBoundaryNodeSet',datestr(now,' mm-dd-yyyy HH-MM-SS'),'.txt'];
    writematrix(exportIVDBoundary,fileName3,'Delimiter',',');
    data3=readlines(fileName3);
    ix3=strlength(data3)>0;
    data3(ix3)=strcat(data3(ix3),",");
    writematrix(data3,fileName3,'QuoteStrings','none');
end
% Export node set for the boundary between the Nucleus and Annulus
if strcmp(exportNucleusBoundary,'on')==1
    path='C:\Users\bazz0003\OneDrive - Flinders\Documents 1\,Laptop\Project\5.
Methods\MATLAB\Create Node-Element Sets\Export - Nucleus Boundary Node\';

    fileName4=[path,'AnnulusNucleusBoundary',datestr(now,' mm-dd-yyyy HH-MM-SS'),'.txt'];
    writematrix(exportNodeNucleusBoundary,fileName4,'Delimiter',',');
    data4=readlines(fileName4);
    ix4=strlength(data4)>0;
    data4(ix4)=strcat(data4(ix4),",");
    writematrix(data4,fileName4,'QuoteStrings','none');
end
```

Appendix D: Python Scripts for Post Processing

Batch.py Python Script

```
# Note that the folder of the Python code should have:
#    - Batch.py Python Code
#    - Data_Extraction.py Python Code
#    - Folder named "Input Files" (Put the Abaqus Input files in this folder)
# Does not require an Abaqus GUI license

import subprocess
import numpy as np
from datetime import datetime
import time
import os
import shutil

# The time taken for each simulation is recorded
start = time.time()

# Get the working directory for the current folder
folderPath = os.getcwd()
filePath = os.getcwd() + "\\Input Files\\"
postProcessing = os.getcwd() + "\\Data_Extraction.py"
postProcessingName = 'Data_Extraction.py'

# Create a new folder in the "Input Files" folder which will store the Abaqus results
today = datetime.now()
mainFolderPath = filePath + "Date - "+datetime.now().strftime("%m-%d-20%y %H-%M-%S")
os.mkdir(mainFolderPath)

# Raise an error if no input files are found in the "Input Files" folder
inputFile = [file for file in os.listdir(filePath) if file.endswith(".inp")]
if len(inputFile) == 0:
    raise Exception("No Input Files Detected")

# For each input file in the batch, run them one after the other
for i in inputFile:
    # Create a new sub-folder for each input file
    s = os.path.splitext(i)
    subFolderPath = mainFolderPath + "\\" + s[0]
    os.mkdir(subFolderPath)
    # Change the directory to the sub-folder
    owk = filePath + "\\" + i
    shutil.copy2(owk,subFolderPath)
    shutil.copy2(postProcessing,subFolderPath)
    os.chdir(subFolderPath)

    print(subFolderPath)

    # Run the Abaqus input file through the Abaqus Standard solver
    # Runs on 4 CPU cores, and interactive option is enabled to provide updates in the
command prompt
    subprocess.run("abaqus job={} cpus=4 interactive".format(s[0]),shell=True)
```

```
    middle = time.time()
    secondsTotal = middle-start
    print("Run Time: "+time.strftime("%H:%M:%S", time.gmtime(secondsTotal))+" (Simulation
Time)")

    # Run the postprocessing script through Abaqus Standard
    subprocess.run('abaqus python {}'.format(postProcessingName),shell=True)

# Print the total time for all simulations
end = time.time()
secondsTotal2 = end-start
print("Run Time: "+time.strftime("%H:%M:%S", time.gmtime(secondsTotal2))+" (Batch
Script)")
```

Data_Extraction.py Python Script

```
# Import all relevant libraries and modules
# Does not require an Abaqus GUI license
from abaqusConstants import *
from odbAccess import *
import numpy as np
from operator import attrgetter
import time
import os

# To reduce script runtime, frequently used objects were initially defined as variables.
# Methods were then used on the variables to access specific data.
# E.g. The displacements for all nodes was initially defined as an object in variable U_I
{U_I = odbStep[odbStepName[i]].frames[j].fieldOutputs['U']}
#      To access certain node sets, a method was used on the U_I variable {U1 =
U_I.getSubset(region=loadNode).bulkDataBlocks}
# This was significantly faster than creating the object everytime that specific data
needed to be extracted.

start = time.time()

# Find the name of the Abaqus input file that was run
fileLocation=os.getcwd()
fileNameFull = [file for file in os.listdir(fileLocation) if file.endswith(".inp")]
fileName = os.path.splitext(fileNameFull[0])[0]

# Open the odb database and assign to variable "odb"
# The variable "odb" will be used to access the members/methods
odbName=fileName+'.odb'
odb=openOdb(path=odbName,readOnly=False)

# Node Set objects for all node sets used in post-processing
nset1 = odb.rootAssembly.instances['L1L2INST'].nodeSets['L1L2']
loadNode = odb.rootAssembly.nodeSets['LOADNODE']
holdNode = odb.rootAssembly.nodeSets['HOLDNODE']
nucleusCentre = odb.rootAssembly.nodeSets['NUCLEUS_CENTRE']
annulusOuterLateral = odb.rootAssembly.nodeSets['ANNULUS_OUTER_LATERAL']
annulusOuterAnterior = odb.rootAssembly.nodeSets['ANNULUS_OUTER_ANTERIOR']
annulusInnerAnterior = odb.rootAssembly.nodeSets['ANNULUS_INNER_ANTERIOR']
ivdTop = odb.rootAssembly.nodeSets['IVD_TOP']
ivdBottom = odb.rootAssembly.nodeSets['IVD_BOTTOM']

## Element Set objects for all element sets used in post-processing
elsetNuc = odb.rootAssembly.instances['L1L2INST'].elementSets['L1L2NUCLEUS']
elsetAnn = odb.rootAssembly.instances['L1L2INST'].elementSets['L1L2ANN']

odbStep = odb.steps # Create a new object for all steps in output databse
odbStepName = odbStep.keys() # Obtain the name of each step

# Find number of frames in each step
odbFrames = np.zeros((len(odbStepName),1))
for i in range(len(odbStepName)):
    frameInStep = len(odbStep[odbStepName[i]].frames)
```

```
    odbFrames [i,0] = frameInStep
# Find the total number of frames for all steps in the entire simulation
totalFrames = int(np.sum(odbFrames))

# For each frame, find the time after the start of the simulation
# Abaqus provides a step time, however this is the time after the start of each step
# Create a numpy array with
#   Column 1: Time (s)
#   Column 2: Step Number
t=np.zeros((totalFrames,2))
indexFirst = 0
indexLast = 0
indexLastStepTime = 0
for i in range(len(odbStepName)):
    # Obtain the step time for all frames, in the given step
    frameInStep2 = odbStep[odbStepName[i]].frames
    stepTime = map(attrgetter('frameValue'),frameInStep2)

    # Find the first and last index for the rows in the "t" array where the step time will
be copied
    numOfStepTime = len(stepTime)
    indexLast = indexFirst + numOfStepTime

    # Copy the step time into the first column of the "t" array
    t[indexFirst:indexLast,0] = stepTime
    # To give the time from the start of the simulation, add the time at the end of the
previous step
    t[indexFirst:indexLast,0] += indexLastStepTime

    # Copy the step number into the second column of the "t" array
    t[indexFirst:indexLast,1]= i+1

    # Increment all indexes
    indexLastStepTime = t[indexLast-1,0]
    indexFirst += numOfStepTime

# The pore pressure output will be obtained at the integration points of all elements
# For each step, the pore pressure output will be obtained for all integration points
# An average and maximum pore pressure output will then be obtained across all integration
points for all steps
num_IntegrationPoints_NP = len(odbStep[odbStepName[0]].frames[-
1].fieldOutputs['POR'].getSubset(region=elsetNuc,position=INTEGRATION_POINT,elementType='C
3D8P').values)
num_Elements_NP = len(elsetNuc.elements)
num_Elements_AF = len(elsetAnn.elements)

# Initialise all local output arrays
POR = np.zeros((num_IntegrationPoints_NP,totalFrames)) #Columns have all frames, rows have
all integration points
POR_Nucleus_Centre = np.zeros((totalFrames,1))
RF = np.zeros((totalFrames,3))
U = np.zeros((totalFrames,3))
U_AF_OuterLateral = np.zeros((totalFrames,3))
U_AF_OuterAnterior = np.zeros((totalFrames,3))
U_IVD_Top = np.zeros((totalFrames,3))
```

```
U_IVD_Bottom = np.zeros((totalFrames,3))
U_NP_Centre = np.zeros((totalFrames,3))
VOL_NP = np.zeros((num_Elements_NP,totalFrames))
VOL_AF = np.zeros((num_Elements_AF,totalFrames))

## Extract field outputs for all frames in all steps
# The bulkDataBlocks method is used to read all the output in bulk form
indexFrame=0
for i in range(len(odbStepName)): #Loop through all steps
    for j in range(int(odbFrames[i,0])): #Loop through all frames in each step

        # Define field output objects as variables
        POR_I = odbStep[odbStepName[i]].frames[j].fieldOutputs['POR']
        RF_I = odbStep[odbStepName[i]].frames[j].fieldOutputs['RF']
        U_I = odbStep[odbStepName[i]].frames[j].fieldOutputs['U']
        EVOL_I = odbStep[odbStepName[i]].frames[j].fieldOutputs['EVOL']

        ## Pore Pressure
        POR_Nucleus =
POR_I.getSubset(region=elsetNuc,position=INTEGRATION_POINT,elementType='C3D8P').bulkDataBl
ocks
        POR[:,indexFrame]=POR_Nucleus[0].data[:,0]

        POR_Nucleus_Centre2 =
POR_I.getSubset(region=nucleusCentre,position=ELEMENT_NODAL).bulkDataBlocks
        POR_Nucleus_Centre[indexFrame,:] = np.average(POR_Nucleus_Centre2[0].data)

        ## Reaction Force
        RF1 = RF_I.getSubset(region=holdNode).bulkDataBlocks
        RF[indexFrame,:] = RF1[0].data[:,:]

        ## Displacement
        U1 = U_I.getSubset(region=loadNode).bulkDataBlocks
        U[indexFrame,:] = U1[0].data[:,:]

        U2 = U_I.getSubset(region=annulusOuterAnterior).bulkDataBlocks
        U_AF_OuterAnterior[indexFrame,:] = U2[0].data[:,:]

        U3 = U_I.getSubset(region=annulusOuterLateral).bulkDataBlocks
        U_AF_OuterLateral[indexFrame,:] = U3[0].data[:,:]

        U4 = U_I.getSubset(region=ivdTop).bulkDataBlocks
        U_IVD_Top[indexFrame,:] = U4[0].data[:,:]

        U5 = U_I.getSubset(region=ivdBottom).bulkDataBlocks
        U_IVD_Bottom[indexFrame,:] = U5[0].data[:,:]

        U6 = U_I.getSubset(region=nucleusCentre).bulkDataBlocks
        U_NP_Centre[indexFrame,:] = U6[0].data[:,:]

        ## Element Volumes
        VOL_NUC1 = EVOL_I.getSubset(region=elsetNuc,elementType='C3D8P').bulkDataBlocks
        VOL_NP[:,indexFrame]=VOL_NUC1[0].data[:,0]

        VOL_ANN1 = EVOL_I.getSubset(region=elsetAnn,elementType='C3D8P').bulkDataBlocks
```

```
        VOL_AF[:,indexFrame]=VOL_ANN1[0].data[:,0]

        indexFrame += 1

# Find the total volume of all elements in NP and AF, for all steps in all frames
totalVolumeNP = np.sum(VOL_NP,axis=0)
totalVolumeAF = np.sum(VOL_AF,axis=0)

output = np.zeros((totalFrames,18))

# The outputs include (Columns 1-17):
#   C1: Time (s)
#   C2: Time (h)
#   C3: Step number
#   C4: Average Pore Pressure in all NP elements (MPa)
#   C5: Maximum Pore Pressure in all NP elements (MPa)
#   C6: Pore Pressure in NP Centre (MPa)
#   C7: Fx (N) at bottom of inferior vertebrae
#   C8: Fy (N) at bottom of inferior vertebrae
#   C9: Fz (N) at bottom of inferior vertebrae
#   C10: Tx (N) at top of superior vertebrae
#   C11: Ty (N) at top of superior vertebrae
#   C12: Tz (N) at top of superior vertebrae
#   C13: Change in volume of all NP elements
#   C14: Change in volume of all AF elements
#   C15: x-displacement of node on outer anterior region of AF (mm)
#   C16: y-displacement of node on outer lateral-most region of AF (mm)
#   C17: Change in IVD disc height (mm)
#   C18: z-displacement of node on centre of IVD (mm)

output[:,0] = t[:,0]
output[:,1] = np.divide(output[:,0],3600)
output[:,2] = t[:,1]
output[:,3] = POR.mean(axis=0)
output[:,4] = POR.max(axis=0)
output[:,5] = POR_Nucleus_Centre[:,0]
output[:,6:9] = RF[:,0:3]
output[:,9:12] = U[:,0:3]
output[:,12] =
np.multiply(np.divide(np.subtract(totalVolumeNP[:],totalVolumeNP[0]),totalVolumeNP[0]),100
)
output[:,13] =
np.multiply(np.divide(np.subtract(totalVolumeAF[:],totalVolumeAF[0]),totalVolumeAF[0]),100
)
output[:,14] = U_AF_OuterAnterior[:,0]
output[:,15] = U_AF_OuterLateral[:,1]
output[:,16] = U_IVD_Top[:,2] - U_IVD_Bottom[:,2]
output[:,17] = U_NP_Centre[:,2]

# Save the extracted output to an Excel file
title = 'Time (s),Time (h),Step No.,Average Pore Pressure in NP (MPa),Maximum Pore
Pressure in NP (MPa),Pore Pressure in NP Centre (MPa),Fx (N),Fy (N),Fz (N),Tx (mm),Ty
(mm),Tz (mm),NP Volume Change (%),AF Volume Change (%),AF Outer Anterior x-displacement
(mm),AF Outer Lateral y-displacement (mm),IVD Height Change (mm),IVD Centre z-displacement
(mm)'
```

```
np.savetxt(fileLocation + "\\" + fileName +
'.csv',output,delimiter=',',newline='\n',header=title,comments='')

end = time.time()
secondsTotal2 = end-start
# Print the time taken for the postprocessing script
print("Run Time: "+time.strftime("%H:%M:%S", time.gmtime(secondsTotal2))+"
(Data_Extraction Script)")
```